This is a preprint, the final version is subject to change, of the American Mineralogist (MSA)
Cite as Authors (Year) Title. American Mineralogist, in press.
DOI: https://doi.org/10.2138/am-2020-7162

Revision 3

The effects of solid-solid phase equilibria on the oxygen fugacity of the upper mantle*

Edward M. Stolper[1], Oliver Shorttle[1,2], Paula M. Antoshechkina[1], and Paul D. Asimow[1]

[1]Division of Geological and Planetary Sciences, California Institute of Technology, Pasadena California, USA
[2]Department of Earth Sciences and Institute of Astronomy, University of Cambridge, Cambridge, UK

Abstract

Decades of study have documented several orders of magnitude variation in the oxygen fugacity (fO_2) of terrestrial magmas and of mantle peridotites. This variability has commonly been attributed either to differences in the redox state of multivalent elements (e.g., Fe^{3+}/Fe^{2+}) in mantle sources or to processes acting on melts after segregation from their sources (e.g., crystallization or degassing). We show here that the phase equilibria of plagioclase, spinel, and garnet lherzolites of constant bulk composition (including whole-rock Fe^{3+}/Fe^{2+}) can also lead to systematic variations in fO_2 in the shallowest ~100 km of the mantle.

Two different thermodynamic models were used to calculate fO_2 vs. pressure and temperature for a representative, slightly depleted peridotite of constant composition (including total oxygen). Under subsolidus conditions, increasing pressure in the plagioclase-lherzolite facies from 1 bar up to the disappearance of plagioclase at the lower pressure limit of the spinel-lherzolite facies leads to an fO_2 decrease (normalized to a metastable plagioclase-free peridotite of the same composition at the same pressure and temperature) of ~1.25 orders of magnitude. The spinel-lherzolite facies defines a minimum in fO_2, and increasing pressure in this facies has little influence on fO_2 (normalized to a metastable spinel-free peridotite of the same composition at the same pressure and temperature) up to the appearance of garnet in the stable assemblage. Increasing pressure across the garnet-lherzolite facies leads to increases in fO_2 (normalized to a metastable garnet-free peridotite of the same composition at the same pressure and temperature) of ~1 order of magnitude from the low values of the spinel-lherzolite facies. These changes in

* This manuscript comprises material presented by the first author in the Roebling Medal lecture given October 24, 2017 Geological Society of America meeting in Seattle.

This is a preprint, the final version is subject to change, of the American Mineralogist (MSA)
Cite as Authors (Year) Title. American Mineralogist, in press.
DOI: https://doi.org/10.2138/am-2020-7162

normalized fO_2 reflect primarily the indirect effects of reactions involving aluminous phases in the peridotite that either produce or consume pyroxene with increasing pressure: Reactions that produce pyroxene with increasing pressure (e.g., forsterite + anorthite ⇌ Mg-Tschermak + diopside in plagioclase lherzolite) lead to dilution of Fe^{3+}-bearing components in pyroxene and therefore to decreases in normalized fO_2, whereas pyroxene-consuming reactions (e.g., in the garnet stability field) lead initially to enrichment of Fe^{3+}-bearing components in pyroxene and to increases in normalized fO_2 (although this is counteracted to some degree by progressive partitioning of Fe^{3+} from the pyroxene into the garnet with increasing pressure). Thus, the variations in normalized fO_2 inferred from thermodynamic modeling of upper mantle peridotite of constant composition are primarily passive consequences of the same phase changes that produce the transitions from plagioclase→spinel→garnet lherzolite and the variations in Al content in pyroxenes within each of these facies. Because these variations are largely driven by phase changes among Al-rich phases, they are predicted to diminish with the decrease in bulk Al content that results from melt extraction from peridotite, and this is consistent with our calculations.

Observed variations in FMQ-normalized fO_2 of primitive mantle-derived basalts and peridotites within and across different tectonic environments probably mostly reflect variations in the chemical compositions (e.g., Fe^{3+}/Fe^{2+}or bulk O_2 content) of their sources (e.g., produced by subduction of oxidizing fluids, sediments, and altered oceanic crust or of reducing organic material; by equilibration with graphite- or diamond-saturated fluids; or by the effects of partial melting). However, we conclude that in nature the predicted effects of pressure- and temperature-dependent phase equilibria on the fO_2 of peridotites of constant composition are likely to be superimposed on variations in fO_2 that reflect differences in the whole-rock Fe^{3+}/Fe^{2+} ratios of peridotites and therefore that the effects of phase equilibria should also be considered in efforts to understand observed variations in the oxygen fugacities of magmas and their mantle sources.

This is a preprint, the final version is subject to change, of the American Mineralogist (MSA)
Cite as Authors (Year) Title. American Mineralogist, in press.
DOI: https://doi.org/10.2138/am-2020-7162

Introduction

There has been longstanding interest in the oxygen fugacity (fO_2) of mantle-derived magmas and their sources (e.g., Osborn, 1959; Buddington and Lindsley, 1964; Haggerty, 1976; Arculus, 1985; Carmichael, 1991; Frost and Lindsley, 1991; Wood, 1991; Frost and McCammon, 2008). This interest reflects the potential importance of the effects of variations in fO_2 on the crystallization sequences and liquid lines of descent of magmas (e.g., Osborn, 1959; Hamilton and Anderson, 1967; Berndt et al., 2004); the variations in fO_2 that can be produced by crystallization differentiation of magmas (e.g., Frost and Lindsley, 1991; Kelley and Cottrell, 2012; Birner et al., 2018; Tang et al., 2018); the insights that observed variations in fO_2 (or their absence) can give into processes affecting the mantle source regions of magmas through space and time (e.g., Arculus, 1985; Ballhaus et al., 1990; Wood, 1991; Li and Lee, 2004; Lee et al., 2005; Frost and McCammon, 2008; Cottrell and Kelley, 2011; Cottrell and Kelley, 2013; Stagno et al., 2013; Brounce et al., 2014; Brounce et al., 2015; Gaillard et al., 2015; Shorttle et al., 2015; Aulbach and Stagno, 2016; Gaetani, 2016; Bénard et al., 2018b; Birner et al., 2018); and the potential feedbacks between magmatic fO_2 and geological processes involving the atmosphere and ocean (e.g., Kasting et al., 1993; Delano, 2001; Kump and Barley, 2007; Frost and McCammon, 2008; Gaillard et al., 2011; Hirschmann, 2012; Gaillard et al., 2015; Brounce et al., 2017; Stolper and Keller, 2018; Stolper and Bucholz, 2019).

As a result of this interest, there have been many studies aimed at quantifying the fO_2 levels recorded by igneous rocks. These studies have been based primarily on determinations of the ratios of oxidized to reduced states of multivalent elements in glasses, whole rocks, or coexisting minerals, from which fO_2 can then be quantified via experimental calibration and thermodynamic modeling. Several elements have been used to determine (or infer) variations in fO_2 (e.g., Cr, Cu, Eu, Fe, S, V), but most such measurements for terrestrial magmas and their sources are based on the oxidation state of Fe (i.e., the Fe^{3+}/Fe^{2+} ratio). These studies have documented variations of up to several orders of magnitude in the fO_2 levels of magmas and mantle peridotites relative to standard oxygen buffer assemblages (e.g., Haggerty, 1976; Arculus,

This is a preprint, the final version is subject to change, of the American Mineralogist (MSA)
Cite as Authors (Year) Title. American Mineralogist, in press.
DOI: https://doi.org/10.2138/am-2020-7162

1985; Christie et al., 1986; Mattioli et al., 1989; Ballhaus et al., 1990; Carmichael, 1991; Frost and Lindsley, 1991; Wood, 1991; Frost and McCammon, 2008; Kelley and Cottrell, 2009; Cottrell and Kelley, 2011; Stagno et al., 2013; Brounce et al., 2014; Moussallam et al., 2014; Shorttle et al., 2015; Miller et al., 2016; Moussallam et al., 2016; Brounce et al., 2017; Hartley et al., 2017; Bénard et al., 2018b; Birner et al., 2018; Tang et al., 2018).

Many explanations have been offered for the variations in fO_2 observed among magmas and peridotites. Most if not all of these factors probably play a role, including the following: (1) Magmatic fO_2 may be inherited from mantle sources that differ in composition (including Fe^{3+}/Fe^{2+} ratio). Such source variations could be due to previous melting events (e.g., Wood, 1991; Bénard et al., 2018b; Birner et al., 2018); to addition of recycled components (or metasomatic agents derived from such components) that were oxidized in near-surface environments prior to recycling (e.g., Mattioli et al., 1989; Ballhaus et al., 1990; Carmichael, 1991; Parkinson and Arculus, 1999; Mungall, 2002; Kelley and Cottrell, 2009; Brounce et al., 2014; Brounce et al., 2015; Gaillard et al., 2015; Shorttle et al., 2015; Waters and Lange, 2016; Brounce et al., 2017; Bénard et al., 2018a; Bénard et al., 2018b; Stolper and Keller, 2018; Moussallam et al., 2019; Stolper and Bucholz, 2019); or to equilibration with or addition of graphite- or diamond-saturated C-O-H fluids, carbonates, or carbonate-silicate melts over ranges of pressure (P) and temperature (T) prior to, synchronous with, or after melting (Eggler, 1983; Blundy et al., 1991; Wood, 1991; Stagno et al., 2013). (2) The action of processes such as crystallization and degassing on mantle-derived melts after segregation from their sources may generate residual liquids that differ in fO_2 relative to their parent liquids and sources (e.g., Mathez, 1984; Carmichael, 1991; Frost and Lindsley, 1991; Lee et al., 2005; Burgisser and Scaillet, 2007; Lee et al., 2010; Kelley and Cottrell, 2012; Lee et al., 2014; Grocke et al., 2016; Moussallam et al., 2016; Brounce et al., 2017; Hartley et al., 2017; Birner et al., 2018; Tang et al., 2018; Moussallam et al., 2019). Or (3) variations in fO_2 may result from heterogeneous equilibria among phases in subsolidus and partially molten mantle peridotites that shift with varying P and T, leading to variations in fO_2 even at constant bulk composition. Examples of

This is a preprint, the final version is subject to change, of the American Mineralogist (MSA)
Cite as Authors (Year) Title. American Mineralogist, in press.
DOI: https://doi.org/10.2138/am-2020-7162

this include redistribution of components (including Fe^{3+} and Fe^{2+}) between coexisting solid, liquid, and fluid phases with changing *P* and *T*; addition or subtraction of phases from the assemblage as phase boundaries are crossed; or shifts in the equilibrium constants of redox equilibria with *P* and *T* such that fO_2 can vary relative to standard redox buffers even when all the phases and their compositions in an assemblage are unchanged (e.g., Wood et al., 1990; Frost, 1991; O'Neill et al., 1993; Ballhaus and Frost, 1994; Ballhaus, 1995; Gudmundsson and Wood, 1995; Woodland and Koch, 2003; Rohrbach et al., 2007; Frost and McCammon, 2008; Stagno and Frost, 2010; Stagno et al., 2013; Jennings and Holland, 2015; Gaetani, 2016; Miller et al., 2016; Birner et al., 2018; Sorbadere et al., 2018).

The focus of this paper is the third of these possibilities: an assessment of variations in fO_2 that may result from heterogeneous equilibria among phases in subsolidus mantle peridotites that shift with varying *P* and *T*. In particular, we evaluate the possibility that significant variations in the fO_2 of a subsolidus mantle peridotite can result from changes in the Fe^{3+} concentrations of coexisting phases due to reactions between them, even without any change in whole-rock composition or Fe^{3+}/Fe^{2+} ratio. Such an assessment of the potential variability of the fO_2 of upper-mantle peridotite as functions of *P* and *T* is facilitated by the availability of thermodynamic models that can be used to calculate the abundances and chemical compositions of phases in stable or metastable equilibrium. In this paper we show that the pMELTS (Ghiorso et al., 2002; Antoshechkina and Ghiorso, 2018) and JH-15 (Jennings and Holland, 2015) models predict significant variations in the fO_2 of a representative, slightly depleted mantle peridotite composition under dry, melt-free conditions at $P < 40$ kbar. We also show that the subsolidus variations (both stable and metastable) in fO_2 of peridotite predicted by these models are driven primarily by the same *P*-sensitive phase equilibria that control the stability of plagioclase (*plag*), aluminous spinel (*sp*), and garnet (*gt*) and the shapes in *P*-*T* space of alumina isopleths in low-Ca orthopyroxene (*opx*) and higher-Ca clinopyroxene (*cpx*) in mantle peridotites.

This is a preprint, the final version is subject to change, of the American Mineralogist (MSA)
Cite as Authors (Year) Title. American Mineralogist, in press.
DOI: https://doi.org/10.2138/am-2020-7162

Phase equilibria and their effects on the fO_2 of a closed-system, subsolidus peridotite

We use two independent thermodynamically based approaches – pMELTS (Ghiorso et al., 2002; Antoshechkina and Ghiorso, 2018) and the JH-15 model (Jennings and Holland, 2015) implemented in Perple_X (Connolly, 2009) – to calculate by Gibbs free energy minimization the phase assemblages of a slightly depleted mantle composition ("DMM"; Workman and Hart, 2005) over ranges of 1 bar to 40 kbar in *P* and 1050 to 1600°C in *T*. Each of these two approaches uses Gibbs free energy minimization to determine at a given *P* and *T* the equilibrium phase assemblage, including the abundances and compositions of all stable phases and the chemical potential (μ) of each phase and system component. Implementing JH-15 through Perple_X directly provides the chemical potential of O_2, μO_2, as O_2 is specified as a system component. In pMELTS, μO_2 in the stable assemblage is calculated based on a summation of the chemical potentials of components that represent a balanced reaction with O_2 on one side of the reaction (Asimow and Ghiorso, 1998); in the calculated lowest Gibbs free energy state, all such reactions yield the same μO_2. In both models, the fO_2 of the equilibrium assemblage is then calculated from the equilibrium μO_2, using a *P*-independent but *T*-dependent standard state corresponding to pure O_2 gas at 1 bar. This choice of a standard state for O_2 differs from those chosen for condensed phase components (e.g., Fe_2SiO_4 in *ol*; Fe_3O_4 in *sp*, etc.), which are taken to be both *P* and *T* dependent, but is the typical choice of standard state for gases (Denbigh, 1971).

The bulk composition of the model peridotite used in these calculations has $Fe^{3+}/Fe^{2+} = 0.031$ and FeO* = 8.17 wt. %; Fe is the only multivalent element considered by either model. Each of the two thermodynamic models has strengths and weaknesses, but by comparing their results we can evaluate which features are potentially robust and which are specific to each model and therefore not currently generalizable.

This is a preprint, the final version is subject to change, of the American Mineralogist (MSA)
Cite as Authors (Year) Title. American Mineralogist, in press.
DOI: https://doi.org/10.2138/am-2020-7162

P-T contour plots

Figure 1 superimposes contours (i.e., isopleths) in *P-T* space of constant fO_2 or constant offsets from fO_2 reference states for calculated DMM phase equilibria. In this and all subsequent figures, calculations based on pMELTS are shown on the left (i.e., Figs. 1ace) while calculations based on JH-15 are shown on the right (i.e., Figs. 1bdf)[1]. All calculated phase assemblages described in this paper are melt-free, so below the calculated solidus (shown as a dashed curve in each panel of Fig. 1), the phase assemblages are stable, composed of *ol* (olivine) + *opx* + *cpx* ± *plag* ± *sp* ± *gt*; but above the stable solidus, the liquid phase is suppressed in the calculations, and metastable, melt-free assemblages are shown. The solidus curves (and the liquidus, which is stable in this *P-T* range in the pMELTS calculations) are shown only for reference and have no influence on the calculated equilibria: i.e., phase assemblages and fO_2 isopleths in stable and metastable solid assemblages are un affected as they cross the positions of the stable solidus and liquidus. Calculated phase boundaries between *plag* and *sp* lherzolite ("*plag*-out") and between *sp* and *gt* lherzolite ("*gt*-in") are shown as solid green curves (although minor *sp* is present in the labeled *plag*- and *gt*-lherzolite fields).

The fO_2 values in Figures 1a and 1b are not normalized relative to a buffer; they are contours of absolute $\log_{10}fO_2$, where fO_2 is in bars. For the DMM composition, both models predict overall isothermal increases in fO_2 with *P* from 1 bar to 40 kbar of ~2-3 orders of magnitude at both 1100°C and 1600°C and isobaric increases with *T* from 1100°C to 1600°C of ~4–5 orders of magnitude at both 1 bar and 40 kbar. Such isothermal increases in absolute fO_2 with increasing *P* are by definition monotonic with μO_2 and thus represent oxidation of the assemblages on an absolute thermodynamic scale. Broadly similar increases are predicted for

[1] The output of the two models is provided in tabular form and can be downloaded from http://dx.doi.org/10.22002/D1.1329 or https://data.caltech.edu/records/1329. pMELTS results are provided along at 1100 and 1300°C isotherms at intervals of 100 bars from 1 to 40001 bars. JH-15 results are provided at several resolutions, for both completeness and ease of use. The master grid file has full output every 1°C and every 100 bars. The down-sampled grid has results every 100°C and 2000 bars. The 1100 and 1300°C isotherms have results every 100 bars. A README file explains the contents of all supplemental files.

This is a preprint, the final version is subject to change, of the American Mineralogist (MSA)
Cite as Authors (Year) Title. American Mineralogist, in press.
DOI: https://doi.org/10.2138/am-2020-7162

silicate melts of constant composition and for commonly used redox buffers (including the FMQ buffer), reflecting the comparable signs and magnitudes of the standard-state volume and enthalpy changes for redox reactions involving Fe in these systems (e.g., Kress and Carmichael, 1991). Shifts in absolute fO_2 controlled either by homogeneous equilibria in a silicate melt or by heterogeneous equilibria among solid redox buffer assemblages are smooth and monotonic in *P*-*T* space. Figures 1a and 1b, however, show considerable structure, including reversals, high 2nd derivatives, and/or discontinuous changes in the slopes of isopleths at phase boundaries (e.g., at the *plag*-out and *gt*-in boundaries) or over narrow *P* and *T* intervals in which phase abundances and composition change significantly.

In Figures 1c and 1d, the $\log_{10}fO_2$ values of Figures 1a and 1b have been modified by subtracting the $\log_{10}fO_2$ of the FMQ buffer at each *P* and *T*; this normalization is referred to as ΔFMQ or FMQ-normalized fO_2. This normalization removes much of the variation (i.e., the total variation decreases by ~4.5-5 log units) in absolute fO_2 over this *P* and *T* range and brings out trends in *P* that are less clear in Figures 1a and 1b. However, the utility of normalizing fO_2 to a particular buffer when studying trends in *P* and *T* is limited unless the standard-state volume and enthalpy changes of the buffer reaction closely match those of the redox reactions among the dominant phases in the assemblage (e.g., Kress and Carmichael, 1991). This is a potential issue in natural peridotite compositions for which the phase assemblages do not match the phases of the FMQ buffer (e.g., they lack quartz everywhere and do not always contain *sp*) and for which there are interacting continuous and discontinuous reactions involving the aluminous phases (i.e., *plag*, *sp*, and *gt*) and *px* (the abbreviation *px* is used to refer to any pyroxene phase), the effects of which are not fully removed, isolated, or enhanced by this normalization. Nevertheless, normalization to FMQ is standard, so we include it throughout.

In Figures 1e and 1f, we show the same pMELTS- and JH-15-calculated results for the DMM composition as in Figures 1a and 1b, but the $\log_{10}fO_2$ values at each *P* and *T* have been normalized by subtracting the $\log_{10}fO_2$ of an *ol*+*opx*+*cpx*±*sp* assemblage with the same DMM composition. To obtain this reference assemblage, we minimized Gibbs free energy at each *P*

This is a preprint, the final version is subject to change, of the American Mineralogist (MSA)
Cite as Authors (Year) Title. American Mineralogist, in press.
DOI: https://doi.org/10.2138/am-2020-7162

and *T* subject to the constraints that *plag* and *gt* (and liquid) were suppressed in the pMELTS calculation (*sp* is required to be present everywhere in the normalizing assemblage for pMELTS because *sp* is the only host for Cr^{3+} in subsolidus calculations in this model) and that *plag*, *sp*, and *gt* (and liquid) were suppressed in the JH-15 calculation. For the pMELTS model, the normalizing assemblage is the metastable *ol*+*opx*+*cpx*+*sp* assemblage in the *plag*- and *gt*-lherzolite facies; in the *sp*-lherzolite facies, the normalizing assemblage is identical to the stable assemblage and so the normalized $\log_{10}fO_2$ value is exactly zero in this field. For the JH-15 model, the normalizing assemblage under all conditions is a metastable *ol*+*opx*+*cpx* assemblage. The normalizing *ol*+*opx*+*cpx*±*sp* assemblages have no phase appearances or disappearances and limited changes in phase compositions over the *P*-*T* range of interest (although as described in the caption to Figure 4, in the pMELTS model, the sole *px* phase at $T \gtrsim 1300$°C and $P \lesssim 3.7$ kbar is pigeonite rather than *opx* plus a higher-Ca, diopsidic *cpx*). This normalization removes the general trends of oxidation (i.e., increasing absolute fO_2) of the DMM model peridotite seen in Figures 1a and 1b that result from increasing *P* and *T* on the dominant *ol*+*opx*+*cpx* assemblage, and it consequently isolates and emphasizes the effects of subsolidus phase changes involving aluminous phases on the structure of the normalized fO_2 isopleths. Although we have not shown them, ΔFMQ values for the *ol*+*opx*+*cpx*±*sp* assemblages (whether stable or metastable) vary smoothly with *P* and *T* because there are no phase changes in either the FMQ assemblage or the *ol*+*opx*+*cpx*±*sp* assemblages (except, as mentioned above, for the appearance of pigeonite in the pMELTS calculation at the low *P* and high *T*, but this has an almost undetectable effect on the normalized fO_2 – see *i* and *ii* in Figs. 1e, 2a, and 2c). Moreover, the changes in the ΔFMQ values of these *ol*+*opx*+*cpx*±*sp* reference assemblages are small over the *P* range of our calculations because the effects of continuous exchanges of components among *ol*, *opx*, *cpx*, ± *sp* are modest: e.g., at 1300°C over the full 40 kbar range considered, ΔFMQ varies by ~1.4 log units for the *ol*+*opx*+*cpx*+*sp* assemblage based on pMELTS and only ~0.4 log units for the *ol*+*opx*+*cpx* assemblage based on JH-15.

This is a preprint, the final version is subject to change, of the American Mineralogist (MSA)
Cite as Authors (Year) Title. American Mineralogist, in press.
DOI: https://doi.org/10.2138/am-2020-7162

It is clear from Figures 1e and 1f that most of the remaining structure in the fO_2 isopleths after normalization to an *ol*+*opx*+*cpx*±*sp* assemblage of DMM composition (with a total range of ~1.6 log units for the pMELTS model and ~1.2 log units for the JH-15 model) is correlated with *P*-dependent phase equilibria involving the aluminous phases in peridotite. Also, most of the *T* dependence of the fO_2 isopleths shown in Figure 1ab and most of the differences between the results of the pMELTS and JH-15 calculations are removed by the normalization to metastable and stable *ol*+*opx*+*cpx*±*sp* assemblages. The most prominent feature of Figures 1e and 1f is the low-fO_2 "well" associated with the *sp*-lherzolite facies. This and other features are explored in more detail in Figures 2 and 3, which plot various results of the calculated phase equilibria as functions of *P* at 1100°C and 1300°C.

Selected isotherms, stable calculations

The low-fO_2 "well" (or "trough"; Jennings and Holland, 2015) associated with the *sp*-lherzolite facies is most evident when normalized to an isocompositional metastable or stable *ol*+*opx*+*cpx*±*sp* assemblage for DMM (e.g., Figs. 1ef; and Figs. 2ab at 1300°C). For the pMELTS model (Fig. 2a), the fO_2 of the stable *plag*+*ol*+*opx*+*cpx*+*sp* mineral assemblage decreases smoothly by ~1.25 orders of magnitude relative to the metastable *ol*+*opx*+*cpx*+*sp* assemblage as *P* increases across the *plag*-lherzolite facies, reaching a minimum at the boundary between the *plag*- and *sp*-lherzolite facies (note again that for the lowest *P*s, pMELTS predicts the stabilization of pigeonite, but the effect on calculated fO_2 is negligible). As mentioned previously, there is no fO_2 offset between the stable and normalizing assemblages in the *sp*-lherzolite facies because the normalizing *ol*+*opx*+*cpx*+*sp* assemblage is identical to the stable assemblage for the pMELTS model in this facies. Then, beginning at *gt*-in, the fO_2 of the stable *gt*+*ol*+*opx*+*cpx*+*sp* mineral assemblage increases relative to that of the metastable *ol*+*opx*+*cpx*+*sp* assemblage with increasing *P* across the *gt*-lherzolite facies, steeply at first and with a progressively decreasing slope, resulting in a ~1.2 orders of magnitude increase by 40 kbar (and approximately recovering the 1 bar value).

This is a preprint, the final version is subject to change, of the American Mineralogist (MSA)
Cite as Authors (Year) Title. American Mineralogist, in press.
DOI: https://doi.org/10.2138/am-2020-7162

For the JH-15 model (Fig. 2b), the corresponding changes are a decrease of ~1.3 orders of magnitude in the fO_2 of the stable *plag*-bearing assemblage relative to the metastable *ol*+*opx*+*cpx* assemblage as *P* increases across the *plag*-lherzolite facies; a minimum, near-zero, and near-constant fO_2 relative to the metastable *ol*+*opx*+*cpx* assemblage across the whole *sp*-lherzolite facies (the amount of *sp* is approximately constant and <2 %; see Fig. 3b3 for the comparable results at 1100°C); an abrupt increase in fO_2 relative to the metastable *ol*+*opx*+*cpx* assemblage at the appearance of *gt*; and a more gradual increase (with decreasing slope) after the disappearance of *sp* from the stable assemblage up to ~30 kbar across the *gt*-lherzolite facies, peaking at a ~1 order of magnitude increase (i.e., not quite recovering the initial low-*P* value), then decreasing by ~0.1 orders of magnitude as *P* increases further to 40 kbar.

The same shifts can be seen in absolute (i.e., unnormalized) fO_2 and ΔFMQ at 1100°C for both models (Figs. 3a1 and 3b1), although they are superimposed on the *P*-dependent overall trends associated with increasing *P* discussed above in connection with Figure 1. Similar trends in ΔFMQ are shown for the KLB-1 fertile peridotite on stable subsolidus isotherms at 800 and1100°C by Jennings and Holland (2015); this similarity is not surprising given that the same thermodynamic model was used in both cases and because the DMM and KLB-1 bulk compositions, though different, are both relatively fertile.

The modeled 1.0-1.3 orders of magnitude variations in fO_2 shown relative to metastable *ol*+*opx*+*cpx*±*sp* assemblages in Figure 2 are comparable to the individual fO_2 ranges of mid-ocean ridge basalts (e.g., Cottrell and Kelley, 2011; Birner et al., 2018), primitive arc magmas (e.g., Kelley and Cottrell, 2009; Brounce et al., 2014), and abyssal peridotites (e.g., Bryndzia and Wood, 1990; Birner et al., 2018). Thus, although as discussed in the Introduction many processes can – and probably do – influence the oxygen fugacities of mantle peridotites and the magmas generated from them by partial melting, according to our modeling, variations in fO_2 comparable to those observed in suites of mantle-derived rocks and magmas can also arise from the effects on fO_2 of changes in peridotite phase assemblages at constant bulk composition over the *P* range most relevant to terrestrial magma genesis.

This is a preprint, the final version is subject to change, of the American Mineralogist (MSA)
Cite as Authors (Year) Title. American Mineralogist, in press.
DOI: https://doi.org/10.2138/am-2020-7162

Selected isotherms, metastable calculations

We conducted a series of additional thermodynamic modeling exercises that take advantage of the capability to probe metastable states in both the pMELTS and JH-15 models and thereby to assess the effects of individual phases on the calculated variations in fO_2 described above. In Figures 2c and 2d, fO_2 values for the DMM bulk composition normalized to *ol+opx+cpx±sp* assemblages are shown vs. *P* at 1300°C based on calculations in which the three Al-rich phases (*plag*, *sp*, and *gt*) were selectively suppressed (i.e., prevented from appearing in the assemblage) when calculating the equilibria. As pointed out previously, in the pMELTS calculations (Fig. 2c), we are only able to suppress *gt* and *plag* because the presence of Cr^{3+} requires *sp*. In the JH-15 calculations (Fig. 2d), however, we can turn each of the three aluminous phases "on" or "off". In this way, we explored the role that each of the aluminous phases plays in the modeled variations in fO_2 in the stable assemblages.

The key results of these calculations are as follows:

- In pMELTS calculations, when *plag* and *gt* are not allowed to form, the assemblage is everywhere *ol+opx+cpx+sp*, which is also the normalizing assemblage, so the normalized fO_2 for this assemblage is zero over the whole range in *P* (corresponding to the horizontal line at 0 in Fig. 2c). Likewise, the metastable state of DMM calculated with JH-15 in which *plag*, *sp*, and *gt* are all suppressed from the assemblage is *ol+opx+cpx*, which is again the normalizing assemblage, so the normalized fO_2 for this assemblage is also zero over the whole range in *P* (corresponding to the horizontal line at 0 in Fig. 2d).
- The blue curves in Figures 2c and 2d show the model results when we allowed *plag* – but not *gt* (or *sp* in the JH-15 calculations) – to appear in the assemblages. For the JH-15 model (Fig. 2d), *plag* is stable in the metastable assemblage at $P \lesssim 10$ kbar. This metastable assemblage differs from the stable assemblage (Fig. 2b) only in that *sp* is not present, and this has only a small effect because the maximum amount of *sp* in the fully stable calculated assemblage is <2% in the *plag*-lherzolite facies (see Fig. 3b3 for the comparable result at 1100°C). The calculated abundance of *plag* decreases continuously from 1 bar to its disappearance at $P \sim 10$

This is a preprint, the final version is subject to change, of the American Mineralogist (MSA)
Cite as Authors (Year) Title. American Mineralogist, in press.
DOI: https://doi.org/10.2138/am-2020-7162

kbar (i.e., at a slightly higher *P* than the ~9 kbar for *plag*-out calculated for the stable, *sp*-bearing assemblage; Fig. 2b), and this is accompanied by a continuous decrease in the normalized fO_2 of the *plag*-bearing metastable assemblage from 1 bar to the *plag*-out boundary. The shapes of the normalized $\log_{10}fO_2$ and *plag* abundance curves vs. *P* are similar (i.e., both are concave down: compare the blue curves in Figs. 2d [1300°C] and 3b3 [1100°C]). The decrease in *plag* abundance with increasing *P* in the *plag*-lherzolite facies is due to discontinuous reactions of *plag*+*ol*±*sp* to produce aluminous *px* components (e.g., Mg-Tschermak, Ca-Tschermak, and jadeite) ± *sp* (e.g., Green and Hibberson, 1970; Borghini et al., 2009); *plag* disappears when such reactions have generated sufficiently aluminous *px* (±*sp*) to host all the Al in the bulk composition. That allowing the stabilization of *plag* alone, without *sp*, does such a good job at reproducing the trend of decreasing fO_2 with increasing *P* in the fully stable assemblage (compare the fO_2 variation in the *plag* stability field in Figs. 2b and 2d) – and the complete absence of this behavior when *plag* stability is suppressed – demonstrates the essential role of *plag* stability and of phase changes involving *plag* in the decrease in fO_2 with increasing *P* across the *plag*-lherzolite facies based on the JH-15 thermodynamic model. The same analysis applies to the pMELTS calculation shown in Figure 2c: Only when *plag* is allowed to stabilize in the calculations is the decrease in fO_2 associated with the increase in *P* across the *plag*-lherzolite facies observed in the output of the model.

- The orange curve in Figure 2d shows the JH-15 model result when *sp* (but not *plag* or *gt*) is allowed to appear in the assemblage (this discussion applies only to the JH-15 modeling, because *sp* cannot be suppressed in the Cr^{3+}-bearing pMELTS calculations). When it is the only Al-rich phase allowed, JH-15 predicts that *sp* is present in the calculated DMM assemblage over the full *P* range shown in Figure 2d, whereas it is only present at low-to-intermediate *P*s in the stable assemblage (see the orange curve in Fig. 3b3; 1100°C). The persistence of *sp* to high *P* when *gt* is prohibited from being present in the metastable assemblage may reflect in part the energetic favorability of accommodating some of the Cr^{3+}

This is a preprint, the final version is subject to change, of the American Mineralogist (MSA)
Cite as Authors (Year) Title. American Mineralogist, in press.
DOI: https://doi.org/10.2138/am-2020-7162

in *sp* rather than entirely in the *px* phases, which in the calculated stable assemblage would partition strongly into the *gt*. The normalized fO_2 of the *sp*-bearing assemblages in the absence of *plag* or *gt* differs by ≲0.1 log units from the *sp*-absent equilibria. This might seem surprising because *sp* can contain significant Fe^{3+} in the form of solid solution toward magnetite (~3 mole %), but in the JH-15 model the abundance of *sp* is low (≲2 wt. %) even when it is present, and thus its presence or absence has only a minor impact on the concentrations of Fe^{3+}-bearing components in the *px* (see Fig. 4d). This is consistent with an important result of all these calculations: It is the Fe^{3+} contents of the *opx* and *cpx* that exert the dominant control on the fO_2 of peridotite over the *P*-*T* range we have explored. Note that allowing only *sp* to form (in the absence of *plag* or *gt*) slightly increases the fO_2 relative to the *sp*-absent *ol*+*opx*+*cpx* assemblage over almost the full *P* range considered (Fig. 2d). This may reflect that *sp* takes more Cr^{3+} than Fe^{3+} from the *px*, resulting in an increase in the activity of ferric-iron-bearing components in the *px*.

- The purple curves in Figures 2c and 2d show the results when *gt* is allowed to appear in the calculated assemblages. For the JH-15 model (Fig. 2d), *gt* appears in the calculated metastable assemblage at ~14.5 kbar, as opposed to at ~18 kbar in the stable calculation (compare Figs. 2b and 2d), reflecting the suppression of *sp*. As in the stable calculation, the progressive increase in *gt* abundance with increasing *P* is accompanied by a correlated increase in the fO_2 relative to the metastable *ol*+*opx*+*cpx* assemblage. This increase in *gt* abundance with increasing *P* in the absence of *sp* as a reactant is due the reaction of aluminous and non-aluminous *px* components to produce *gt* (e.g., Green and Ringwood, 1970). That allowing the stabilization of *gt* alone in the metastable assemblage does such a good job at reproducing the trend in normalized fO_2 of the truly stable assemblage at P >15 kbar (and that no hint of this behavior is present when *gt* is suppressed; compare the purple curve with the blue and orange curves in Fig. 2d) demonstrates the essential role of *gt* stability and of phase changes involving *gt* in the calculated ~1 order of magnitude increase in fO_2 with increasing *P* across the *gt*-lherzolite facies in the *P* range we have investigated.

This is a preprint, the final version is subject to change, of the American Mineralogist (MSA)
Cite as Authors (Year) Title. American Mineralogist, in press.
DOI: https://doi.org/10.2138/am-2020-7162

The almost discontinuous increase in normalized fO_2 observed in the stable peridotite calculations at ~18 kbar is due to the narrow coexistence interval of *sp*+*gt* in lherzolite and is not present in the metastable calculation where *sp* is suppressed (e.g., compare the purple curve in Fig. 2d with the black curve in Fig. 2b). The same overall analysis applies to the pMELTS calculation shown in Figure 2c: Only when *gt* is allowed to form is there an increase in fO_2 normalized to the metastable *ol*+*opx*+*cpx*+*sp* assemblage across the *P* range of the *gt*-lherzolite facies. Because *sp* cannot be suppressed in the Cr^{3+}-bearing pMELTS model, the purple curve in Figure 2c and the black curve in Figure 2a are identical (except in the *plag* stability field).

The results shown in Figure 2 demonstrate that *plag* and *gt* are essential for generating the large changes in fO_2 observed in the peridotite calculations when they are normalized to the metastable *ol*+*opx*+*cpx*±*sp* DMM assemblages (Figs. 2a-2d). Without their presence, the normalized fO_2 is as low at the *P*s of the *plag*- and *gt*-lherzolite facies as in the *sp*-lherzolite facies. Moreover, the continuous decreases in fO_2 of lherzolite assemblages normalized to the metastable *ol*+*opx*+*cpx*±*sp* assemblages as the *sp*-lherzolite facies is approached, whether with increasing *P* in the *plag*-bearing facies or with decreasing *P* in the *gt*-bearing facies, are highly correlated with the progressive decreases in *plag* or *gt* abundance when these phases are permitted in the assemblage (e.g., compare the curves showing *plag* and *gt* phase abundances in Figs. 3a3 and 3b3 with the normalized fO_2 curves in Figs. 2a and 2b or 2c and 2d).

Variations in fO_2 in the *plag*-lherzolite facies

Coupling between alumina in *px* and fO_2 in the *plag*-lherzolite facies. A clue as to the explanation of the correlations between fO_2 and *P*-dependent reactions involving the abundances of *plag* and *gt* comes from comparing the shapes of the calculated $\log_{10}fO_2$ (normalized to the metastable *ol*+*opx*+*cpx*±*sp* assemblages) vs. *P* curves with those of curves showing the activity of Al_2O_3 in *opx* vs. *P*. For the pMELTS model, this comparison is between Figure 2a and the

This is a preprint, the final version is subject to change, of the American Mineralogist (MSA)
Cite as Authors (Year) Title. American Mineralogist, in press.
DOI: https://doi.org/10.2138/am-2020-7162

heavier curve showing Al_2O_3 activity in Figure 2e, and a similar comparison may be made between Figures 2b and 2f for the JH-15 model: As the normalized $\log_{10} fO_2$ goes down with increasing *P* across the *plag*-lherzolite facies, remains constant across the *sp*-lherzolite facies, and then rises again across the *gt*-lherzolite facies, the activity of Al_2O_3 in the *opx* is anti-correlated with these changes. This is consistent with the correlations discussed above between fO_2 and modal abundance of *plag* and *gt* in the model peridotite assemblages (Figs. 3a3 and 3b3 at 1100°C) because the abundances of these phases are connected to transfers of Al_2O_3 into and out of *px*.

In the *plag*-lherzolite facies, the Al_2O_3 content of *px* goes up with increasing *P* at constant *T* due primarily to the following continuous reactions, which go to the right with increasing *P*:

$$\begin{aligned} &\tfrac{1}{3} \text{ fayalite } (ol) + \tfrac{2}{3} \text{ anorthite } (plag) \\ &= \tfrac{1}{2} \text{ Fe-Tschermak } (px) + \tfrac{1}{2} \text{ hedenbergite } (cpx), \end{aligned} \quad (1)$$

and

$$\begin{aligned} &\tfrac{1}{3} \text{ fayalite } (ol) + \tfrac{2}{3} \text{ anorthite } (plag) \\ &= \tfrac{1}{2} \text{ Ca-Tschermak } (px) + \tfrac{1}{2} \text{ ferrosilite } (opx), \end{aligned} \quad (2)$$

where Fe-Tschermak and Ca-Tschermak refer, respectively, to the $Fe^{2+}Al_2SiO_6$ and $CaAl_2SiO_6$ components in *px*. These and other numbered reactions are balanced based on end-member component formula units containing a single oxygen (e.g., the formula unit of fayalite is $Fe_{½}Si_{¼}O$); given this choice, the total numbers of formula units on both sides of the reactions are equal and the coefficients on both sides of the balanced reactions always sum to one. Although these reactions are more typically written in terms of Mg-bearing end members, we have chosen to focus on the Fe^{2+}-bearing end members for consistency with the graphical analysis presented below. Note that neither reaction (1) nor (2) is a redox reaction. All of the Al atoms in *plag* are tetrahedrally coordinated by oxygen, but half of the Al in Al-bearing *px* components is octahedrally coordination by oxygen; thus, consistent with the generalization that structures with octahedrally coordinated Al have lower volumes than those with tetrahedrally coordinated Al,

This is a preprint, the final version is subject to change, of the American Mineralogist (MSA)
Cite as Authors (Year) Title. American Mineralogist, in press.
DOI: https://doi.org/10.2138/am-2020-7162

the standard-state volume changes of both these reactions is negative, so the right-hand sides of these equilibria are favored with increasing *P*. The generation of Al-bearing *px* components by Tschermak substitution at the expense of *ol* and *plag* results in increasing Al_2O_3 content of the *px* (and hence in the Al_2O_3 activity in the *opx*; Figs. 2e and 2f) as *P* increases across the *plag*-lherzolite facies and the negatively sloped alumina-in-*px* isopleths in *P*-*T* space are traversed (e.g., Obata, 1976; Gasparik, 2014). Figures 3a3 and 3b3 show the magnitude of this effect at 1100°C on the amount of *px* in the peridotite based on the pMELTS and JH-15 models: For both models, the calculated abundances of *cpx* and *opx* increase by >100% and 20–25%, respectively, from ~1 bar to *plag*-out. These large increases are not surprising because all the *plag* in the assemblage at 1 bar (~10 wt. %) plus an equal amount of *ol* has to be replaced mainly by *px* when the *plag*-out boundary is reached.

How does this relate to fO_2? At 1 bar, most of the Fe^{3+} in the model peridotite is contained in the *px* (in JH-15, the fraction of the total Fe^{3+} in DMM contained in *sp* is only ~1.5 % [Fig. 4b], whereas in pMELTS it is tens of percent [Figs. 4a]), and this remains the case throughout the *plag*-lherzolite facies. Thus, the generation of additional *px* molecules on the right-hand sides of reactions (1) and (2) as *P* increases leads to progressive dilution of the Fe^{3+} in *px*, lowering both the concentrations (Figs. 2g and 2h, and 3a2 and 3b2) and activities (Fig. 2e and 2f) of their Fe^{3+}-bearing components, which in turn will generally lead to decreasing fO_2 relative to the metastable *ol*+*opx*+*cpx*±*sp* assemblages. Although the pMELTS and JH-15 models differ in their details – particularly in the abundance of *sp* (compare the orange curves in Figs. 3a3 and 3b3) and the proportion of the Fe^{3+} in the *sp* (Fig. 4a and 4b) – for both models the dilution of Fe^{3+}-bearing components in *px* is the primary factor in the decrease in fO_2 relative to the *plag*-absent metastable assemblages with increasing *P* in the *plag*-lherzolite facies. It is important to emphasize that Fe^{3+} is basically a passive actor in this process: The absolute quantity of Fe^{3+} in the peridotite is fixed and in both models it is mostly contained in *px* across the full *P* range of the *plag*-lherzolite facies; hence its concentration in the *px* is determined by the *P*-dependent transfer of Al from tetrahedral coordination in the *plag* to partly octahedral coordination in the

This is a preprint, the final version is subject to change, of the American Mineralogist (MSA)
Cite as Authors (Year) Title. American Mineralogist, in press.
DOI: https://doi.org/10.2138/am-2020-7162

px, which increases the total mass of *px,* decreases the concentration of Fe^{3+} (and therefore the activities of Fe^{3+}-bearing components in the *px*), and thereby decreases fO_2 by ~1.2-1.3 orders of magnitude normalized to the metastable *ol*+*opx*+*cpx*±*sp* assemblages; similar effects are seen in the trends of absolute fO_2 and ΔFMQ (Figs. 3a1 and 3b1).

Note that there can be departures from the general rules stated in the previous paragraph that the activity of Fe_2O_3 (or that of any other Fe^{3+}-bearing component) in a phase correlates positively with its Fe^{3+} concentration (e.g., because the activity coefficient is also changing due to variations in the concentrations of other components in the phase) or that fO_2 necessarily correlates simply with this activity with changing *P* or *T* (e.g., the standard-state free energy changes of reactions by which fO_2 can be calculated vary with *P* and *T*, and such calculations depend on activities of other components, often in other phases, which are also shifting). Despite these potentially confounding factors, this is a widely applied and useful rule of thumb for thinking about how fO_2 will vary with phase compositions (e.g., O'Neill et al., 1993; Ballhaus and Frost, 1994; Ballhaus, 1995; Gudmundsson and Wood, 1995; Woodland and Koch, 2003; Frost et al., 2004; Rohrbach et al., 2007; Frost and McCammon, 2008; Stagno and Frost, 2010) that for the most part successfully rationalizes the results of our thermodynamic modeling. This is especially so when fO_2 is normalized to a metastable DMM *ol*+*opx*+*cpx*±*sp* assemblage, because the bulk composition is identical for both the stable and normalizing assemblages and the phase compositions and proportions are also similar in both assemblages, with the result that most potentially confounding factors will tend to cancel out.

Comparison to previous work (*plag*-bearing assemblages). Ballhaus and Frost (1994) and Ballhaus (1995) developed a related line of reasoning that also predicted that conversion of *plag* lherzolite to *sp* lherzolite would lead to a significant decrease in fO_2. They modeled the stepwise conversion of a fertile *sp* lherzolite to a *plag* lherzolite at 12 kbar and 1230°C via the *sp* + *cpx* + *opx* = *ol* + *plag* reaction (see reaction (3), below), and they assumed that the *sp* contains all the Fe^{3+} in the system. As the reaction proceeds, *sp* is consumed, but never exhausted, and as its abundance decreases in the assemblage, the Fe^{3+} becomes progressively enriched in the

This is a preprint, the final version is subject to change, of the American Mineralogist (MSA)
Cite as Authors (Year) Title. American Mineralogist, in press.
DOI: https://doi.org/10.2138/am-2020-7162

decreasing mass of *sp*, leading to an increase in fO_2 of slightly more than 3 orders of magnitude relative to that of the initial, *plag*-free assemblage. Their calculation thus anticipated the results of our modeling that predicts a higher fO_2 of *plag* lherzolite relative to a *plag*-absent lherzolite at a given *P* and *T*, and they attributed it – as we have also done – to a passive increase in the concentration of Fe^{3+} in the dominant Fe^{3+}-bearing phases (*sp* in their case; *px* in our case) due to reactions that progressively consume *px*±*sp* and produce *ol*+*plag*.

Although conceptually similar, there are differences between our treatment and that of Ballhaus and Frost (1994) and Ballhaus (1995). The most important is that, according to both of the thermodynamic models we consider here, most of the Fe^{3+} in the system resides in *px*, whether the modeled peridotite is in the *plag*- or *sp*-lherzolite facies, whereas the Ballhaus and Frost (1994) model assumes the *sp* is the sole repository of Fe^{3+}. This approximation is inconsistent with our results using the JH-15 model (Fig. 4b) and studies of natural *sp* lherzolites (e.g., Woodland et al., 1992; O'Neill et al., 1993), which together suggest that typically only 10–30 % of the Fe^{3+} resides in *sp*. As a result of this approximation, the decrease in fO_2 upon conversion of *plag* to *sp* lherzolite based on Ballhaus and Frost (1994) and Ballhaus (1995) is 2-3 orders of magnitude larger than what is predicted by our modeling, in which the dilution of Fe^{3+} in the *px* as a result of *px*-producing reactions with increasing *P* across the *plag*-lherzolite field drives this fO_2 change rather than dilution of Fe^{3+} in *sp*. Moreover, as shown in Figure 2d, our results show that this effect is present even when *sp* is not allowed to stabilize in the JH-15 model, demonstrating that for this model *sp* is not the dominant factor in producing a significant decrease in fO_2 relative to the metastable *ol*+*opx*+*cpx* assemblage as *P* increases across the *plag*-lherzolite facies: Indeed, the role of *sp* in this model trend must be almost negligible given that the results are essentially unchanged whether *sp* is or is not allowed to stabilize (compare the *plag*-lherzolite fields in Figs. 2b and 2d). Note, however, that although according to our results the decrease with *P* in fO_2 relative to the metastable *ol*+*opx*+*cpx* assemblage results from the dilution of Fe^{3+} in the *px* by the reaction of *ol*+*plag* to Fe^{3+}-free *px* components rather than from dilution of Fe^{3+} in the *sp*, the Fe^{3+} in the *sp* (when it is allowed to stabilize in our models)

This is a preprint, the final version is subject to change, of the American Mineralogist (MSA)
Cite as Authors (Year) Title. American Mineralogist, in press.
DOI: https://doi.org/10.2138/am-2020-7162

nevertheless does go down with increasing extent of consumption of *ol*+*plag* with increasing *P* in our modeling; this is mostly due to a passive response to the decreasing fO_2 driven by the dilution of Fe^{3+} in the *px* phases. Despite these differences, we emphasize that our results agree with the conclusion of Ballhaus and Frost (1994) and Ballhaus (1995) that conversion of *plag* lherzolite to *sp* lherzolite at a constant *P* and *T* results in a significant decrease in fO_2 and that this reflects a dilution of Fe^{3+} in the dominant phase(s) in which it occurs.

Graphical analysis of the *plag*-lherzolite facies. The model system on which we focus to illustrate graphically the effects on fO_2 of heterogeneous equilibria in peridotites is the five-component system FeO-$Fe_{⅔}O$-CaO-$Al_{⅔}O$-$Si_{½}O$ (i.e., FeO-Fe_2O_3-CaO-Al_2O_3-SiO_2, but all components are expressed on a single-oxygen basis). Although it lacks MgO, we show below that this quinary end-member model system captures the essence of the more complex system modeled using pMELTS and JH-15. The phases of interest for *plag*-, *sp*-, and *gt*-lherzolite facies are *ol* (the fayalite end member, $Fe^{2+}{}_2SiO_4$); *opx* (dominantly the ferrosilite end member, $Fe^{2+}{}_2Si_2O_6$, which is metastable at low *P*; Lindsley et al., 1964); *cpx* (dominantly the hedenbergite end member, $CaFe^{2+}Si_2O_6$,); *plag* (the anorthite end member, $CaAl_2Si_2O_8$); *sp* (the hercynite-magnetite solid solution, $Fe^{2+}Al_2O_4$-$Fe^{2+}Fe^{3+}{}_2O_4$); and *gt* (dominantly the almandine end member, $Fe^{2+}{}_3Al_2Si_3O_{12}$, at the *P*s of we have modeled, in solid solution with smaller amounts of skiagite, $Fe^{2+}{}_3Fe^{3+}{}_2Si_3O_{12}$, and grossular, $Ca_3Al_2Si_3O_{12}$; andradite, $Ca_3Fe^{3+}{}_2Si_3O_{12}$, can be written as a linear combination of these other *gt* end members). Other important components in the *opx* are Fe-Tschermak ($Fe^{2+}Al_2SiO_6$) and Fe-essenite ($Fe^{2+}Fe^{3+}AlSiO_6$), the assumed dominant Fe^{3+}-bearing component, although a "ferro-ferri-*opx*" species ($Fe^{2+}Fe^{3+}{}_2SiO_6$) could also be used as a component. Likewise, other important components in the *cpx* are Ca-Tschermak ($CaAl_2SiO_6$) and Ca-essenite ($CaFe^{3+}AlSiO_6$), the assumed dominant Fe^{3+}-bearing species. Note, however, that all of the components listed for *opx* and *cpx* can be present in both phases, and several can be written as linear combinations of others: e.g., Fe-essenite is an equal mix of the $Fe^{2+}Fe^{3+}{}_2SiO_6$ and Fe-Tschermak end members.

This is a preprint, the final version is subject to change, of the American Mineralogist (MSA)
Cite as Authors (Year) Title. American Mineralogist, in press.
DOI: https://doi.org/10.2138/am-2020-7162

Figure 5a shows the positions of each of the components listed in the previous paragraph projected from fayalite and hedenbergite (i.e., from *ol*+*cpx*) onto the $Si_{½}O$-$Al_{⅔}O$- $Fe_{⅔}O$ plane (except for grossular, which in projection plots below the reference triangle on the extension of the $Si_{½}O$-$Al_{⅔}O$ join); this projection is related to those used in Woodland and O'Neill (1993; 1995). By restricting our consideration to the end-member system projected from fayalite and hedenbergite, the phase relations of all *ol*+*cpx*-bearing assemblages, although schematic, follow the topological rules of a ternary system: In detail, projection from pure hedenbergite preserves the precise projected positions of the end members, whereas projection from the actual Al- and Fe^{3+}-bearing *cpx* composition would preserve exact ternary topology; the difference between these choices is expected to be minor for reasonable peridotite compositions so we choose the simple option of projecting from pure hedenbergite but assuming that the projection preserves ternary topology. Note that that we could lump MgO- and FeO-bearing end members of the ferromagnesian phases (i.e., we could replace the FeO component with an (Mg,Fe)O component). Although the rigor of the topologies of the isothermal sections shown in Figure 5 would be lost (in that the variance would be increased by one in all assemblages), the features of this projection would still provide a useful visualization of the phase relations of an MgO-rich peridotite.

Figure 5b shows schematically the projected *ol*+*cpx*-saturated phase relations for the entire $Si_{½}O$-$Al_{⅔}O$-$Fe_{⅔}O$ plane for conditions under which a model mantle peridotite would be in the *plag*-lherzolite facies. Assemblages containing magnetite-hercynite *sp* are stable over most of the projected composition space, so in order to illustrate the effects of increasing *P* on the fO_2 values of naturally occurring low-Fe^{3+}, *sp*-absent *plag*-lherzolites in which *opx* > *plag* (i.e., near the upper-right edge of the diagram), the relevant low-Fe^{3+} phase relations from Figure 5b are enlarged in Figure 6a. The composition of a model natural peridotite is shown as a green cross (Fig. 5) or dot (Fig. 6). This composition is schematic in Figures 5 and 6; in particular, the bulk Fe^{3+} content ($X_{Fe_{⅔}O}$) is exaggerated so as to illustrate the effects of interest. The bulk composition lies on an *opx*+*plag* tie line in this projection of the four-phase *opx*+*plag*+(*ol*+*cpx*)

This is a preprint, the final version is subject to change, of the American Mineralogist (MSA)
Cite as Authors (Year) Title. American Mineralogist, in press.
DOI: https://doi.org/10.2138/am-2020-7162

stability field in Figures 5b and 6a. (The appearance of "+(*ol*+*cpx*)" at the end of a list of phases indicates that the assemblage contains these two phases and is projected from them in Figures 5 or 6.) The *opx*+*plag* tie lines extend from the projected position of anorthite to the projected edge of the *opx* field (e.g., to the red curves in Figure 6a; these are also positioned arbitrarily so as to illustrate the effects of interest); the important point is that the *opx* compositions are not pure $Fe^{2+}_2Si_2O_6$, but are displaced downwards toward the $Al_{⅔}O$ and $Fe_{⅔}O$ apices, reflecting the incorporation of Al and Fe^{3+} in the *opx*.

The important feature of Figure 6a is the change with increasing *P* in the position of the *opx* end of the *opx*+*plag* tie line that passes through the green dot representing the peridotite bulk composition. As described above, the composition of the *opx* coexisting with *plag* becomes progressively richer in Al with increasing *P*, corresponding to progressive downward movement of the edge of the *opx* field in Figure 6a; i.e., toward the Fe-Tschermak component, which in this projection coincides with pure anorthite. Because the tie lines are radial to anorthite in this projection, the composition of the *opx* simply moves with increasing *P* to higher alumina contents along the tie line extending from anorthite, through the peridotite composition, to the *opx* composition; this is shown by the green arrow moving along this tie line from point *a* to point *b* with increasing *P*. The changing projected position of the *opx* composition relative to the bulk composition illustrates that the *opx*/*plag* ratio increases with increasing *P*, in accordance with our expectations based on reactions (1) and (2) and the output of thermodynamic modeling of the natural peridotite composition shown in Figures 3a3 and 3b3. The dotted black lines close to the projected $Si_{½}O$-$Al_{⅔}O$ edge near the top of Figure 6a represent roughly constant Fe^{3+} concentration (i.e., $X_{Fe_{⅔}O}$); the Fe^{3+} concentration clearly decreases in the *opx* coexisting with *plag*+(*ol*+*cpx*), from point *a* to point *b* as the alumina content (i.e., $X_{Al_{⅔}O}$) of the *opx* increases with increasing *P*. As described above, such decreases in Fe^{3+} concentration will generally lead to a decrease in fO_2 relative to a metastable *ol*+*opx*+*cpx* assemblage.

Figure 6a also demonstrates graphically why transformation at constant *P* and *T* from a metastable *plag*-free assemblage to the stable *plag*-bearing assemblage leads to an increase in

This is a preprint, the final version is subject to change, of the American Mineralogist (MSA)
Cite as Authors (Year) Title. American Mineralogist, in press.
DOI: https://doi.org/10.2138/am-2020-7162

fO_2 relative to the metastable assemblage (as shown for the pMELTS and JH-15 models in Figures 2a-2d). The only aluminous phase in the metastable *ol*+*opx*+*cpx* assemblage that appears in the projection shown in Figure 6a is *opx*. Thus, in this projection, the *opx* in the metastable assemblage coincides with the bulk composition of the peridotite, so both plot at the position of the green dot. When the metastable assemblage transforms to the stable *plag*-bearing assemblage, the green dot representing the bulk composition of the peridotite does not change, and it will lie on a stable *opx*+*plag*+*(ol*+*cpx)* tie line at the *P* and *T* of the transformation. The *opx* composition at the end of a stable *opx*+*plag* tie line passing through the green dot must have a higher Fe^{3+} concentration than the metastable *opx* plotting at the green dot, and hence given our approximation that fO_2 scales with the Fe^{3+} content of the *opx*, the fO_2 of the stable assemblage will be higher than that of the metastable assemblage at the same *P* and *T*.

The graphical analysis based on Figure 6a illustrates the consequences of reactions (1) and (2) and the results of the thermodynamic models, which show increasing Al contents of *px* as *P* increases across the *plag*-lherzolite facies. Neglected degrees of freedom in this assemblage that might change the anti-correlation between $X_{Fe_{2/3}O}$ and $X_{Al_{2/3}O}$ in *opx* are (1) the presence of *sp* in the Cr^{3+}-bearing calculations and (2) exchange of Fe^{3+} and Al^{3+} components between *opx* and *cpx*. The first possibility is discussed in the first part of the next section. Regarding the second possibility, such redistribution is occurring to some degree: For example, Figure 3b2 shows for the JH-15 model that the Fe^{3+} partition coefficients between *opx* and *cpx* and between *sp* and both *px* phases decrease with increasing *P* across the *plag*-lherzolite facies; the Fe^{3+} content of *cpx* actually increases slightly over much of this *P* range while the monotonic decrease of Fe^{3+} in the *opx* is significant. However, the agreement between the phase relations modeled with pMELTS and JH-15 and those portrayed using the projection from *cpx* (which neglects its Fe^{3+} and Al^{3+} contents) suggests that the effects of such redistribution do not overwhelm the simple effects of dilution of the Fe^{3+} in the *opx*, which is the major reservoir of Fe^{3+} in the calculated DMM assemblage under these conditions (Fig. 4b).

This is a preprint, the final version is subject to change, of the American Mineralogist (MSA)
Cite as Authors (Year) Title. American Mineralogist, in press.
DOI: https://doi.org/10.2138/am-2020-7162

The effects of spinel

Stabilization of spinel in the *plag*-lherzolite facies. One aspect of the thermodynamic analysis of natural *plag* lherzolite that is not fully captured by the simplified graphical analysis of Figure 6a is the effect of Cr^{3+} on the stabilization of *sp*. Whereas our analysis of Figure 6a places the model peridotite in the *opx*+*plag*+(*ol*+*cpx*) stability field, Figure 3 shows that both the pMELTS and JH-15 models yield the assemblage *opx*+*plag*+*sp*+*(ol*+*cpx)* throughout the *plag*-lherzolite facies at 1100°C. The reason for this difference between the thermodynamic calculations of the DMM composition and our graphical treatment of a simplified 5-component model system is that Cr^{3+}-rich *sp* is stable everywhere in the *plag*-lherzolite facies based on both the pMELTS and JH-15 models, but given the low Fe^{3+} content of the model composition, in the absence of Cr^{3+}, *sp* would not be present over most of the *plag*-lherzolite facies, in agreement with the schematic phase relations illustrated in Figure 5 (e.g., the *sp*-in boundary at 1100°C is calculated to be only ~1.3 kbar lower than the *plag*-out boundary for this composition based on applying the pMELTS model to a Cr^{3+}-free DMM composition). Also, as emphasized previously, the two thermodynamic models used here differ from each other in their predicted amounts of *sp* in the stable assemblages for the DMM composition at 1100°C: The pMELTS calculation yields ~1.4 wt. % *sp* at 1 bar, increasing progressively to about ~3.9 wt. % when *plag* disappears from the assemblage at ~7.6 kbar (see the orange curve at *P*s less than the *plag*-out boundary in Fig. 3a3); in contrast, JH-15 has considerably lower *sp* abundance (~0.4 wt. % at 1 bar), only beginning at ~6 kbar to increase in abundance significantly to ~2.4 % at *plag*-out at ~8.3 kbar (see the orange curve at *P*s less than the *plag*-out boundary in Fig. 3b3). As indicated previously, the primary reason for these differences in abundance of *sp* between the two calculations is that, whereas for the pMELTS calculations 100% of the Cr^{3+} goes into *sp* — leading to a relatively large amount of Cr^{3+}-rich *sp* throughout the *plag*-lherzolite facies — much of the Cr^{3+} in JH-15 partitions into the *px* (e.g., JH-15 predicts that only ~30-60% of the Cr^{3+} in the system is in *sp* in the *plag*-lherzolite field), resulting in a much lower *sp* abundance until *P*

This is a preprint, the final version is subject to change, of the American Mineralogist (MSA)
Cite as Authors (Year) Title. American Mineralogist, in press.
DOI: https://doi.org/10.2138/am-2020-7162

approaches that of the *plag*-out boundary (compare the orange curves at *P*s less than the *plag*-out boundary in Figs. 3a3 and 3b3).

The effects of the stabilization of *sp* in an Fe^{3+}-bearing but Cr^{3+}-free *plag*-lherzolite facies can be understood using the sequence of projected phase equilibria shown in Figures 5b-5e. Given the low abundance of Fe^{3+} in such a peridotite, throughout most of the *plag*-lherzolite facies a model peridotite composition plots in the four-phase *opx*+*plag*+(*ol*+*cpx*) field, shown in projection by tie lines between anorthite and Al, Fe^{3+}-bearing *opx* (Figs. 5b and 6a). However, more Fe^{3+}- and/or Al-rich compositions will, at the conditions of Figure 5b, stabilize Fe^{3+}-bearing *sp* and plot in the five-phase *opx*+*plag*+*sp*+*(ol*+*cpx)* field, represented by the *opx*+*plag*+*sp*+*(ol*+*cpx)* triangle in Fig. 5b. As illustrated in the progression from Figures 5b to 5f, the *opx* vertex of this triangle sweeps down (reflecting the increasing Al^{3+} content of the *opx*) and to the right with increasing *P*, and the *sp* vertex also sweeps to the right. The stoichiometry of the continuous reaction represented by the *opx*+*plag*+*sp*+*(ol*+*cpx)* triangle moving to the right with increasing *P* is

$$\begin{aligned} &\tfrac{1}{2} \text{ fayalite } (ol) + \tfrac{1}{2} \text{ anorthite } (plag) + \\ &= \tfrac{1}{4} \text{ hercynite } (sp) + \tfrac{3}{8} \text{ hedenbergite } (cpx) + \tfrac{3}{8} \text{ ferrosilite } (opx). \end{aligned} \quad (3)$$

As a consequence, with increasing *P* the model Cr^{3+}-free peridotite moves from the *opx*+*plag*+(*ol*+*cpx*) field at low *P* (Fig. 5b), until a *P* is reached (that depends on its Fe^{3+} content) at which it plots exactly on the *opx*+*plag*+(*ol*+*cpx*) edge of the *opx*+*plag*+*sp*+*(ol*+*cpx)* triangle (Fig. 5c). This point represents the *P* of *sp*-in for the bulk composition shown in Figure 5, but the assemblage is still a *plag* lherzolite.

With further increases in *P*, the *opx*+*plag*+*sp*+*(ol*+*cpx)* triangle continues to move to the right, passing over the peridotite bulk composition, resulting in a hercynite-magnetite *sp* solid solution joining the assemblage; the peridotite assemblage is now a *sp*+*plag* lherzolite (Fig. 5d). Continued rightward movement of the triangle with increasing *P* does not alter the phases in the *sp*+*plag*-lherzolite assemblage as long as the green dot remains within the triangle, but the

This is a preprint, the final version is subject to change, of the American Mineralogist (MSA)
Cite as Authors (Year) Title. American Mineralogist, in press.
DOI: https://doi.org/10.2138/am-2020-7162

abundances of *plag* and *ol* decrease and those of *opx*, *cpx*, and *sp* increase via reaction (3). Just as previously described for reactions (1) and (2), the production of *px* components by reaction (3) dilutes Fe^{3+} in the *px*; the reaction also produces hercynite that dissolves in the *sp*, resulting in a concurrent dilution of the magnetite component in the *sp*. This dilution of Fe^{3+}-bearing components in the *px* and *sp* as the *opx+plag+sp+(ol+cpx)* triangle sweeps over the model peridotite composition results in a progressive decrease in fO_2 relative to a metastable *ol+opx+cpx* assemblage (and in absolute fO_2 and ΔFMQ based on the results on DMM shown in Figs. 3a1 and 3b1) that is related to but not identical to the decrease in fO_2 associated with reactions (1) and (2), because these reactions do not involve production of *sp*. Continued increases in *P* eventually result in the triangle moving far enough to the right that its left edge coincides with the projected bulk composition; the abundance of *plag* in the stable assemblage is zero at this *P* (although the assemblage is still *plag* saturated), corresponding to *plag*-out for this composition (Fig. 5e). As *P* increases beyond this point, the model peridotite plots on *opx+sp+(ol+cpx)* tie lines and is in the *sp*-lherzolite facies (Fig. 5f). Note that throughout the movement to the right of the triangle with increasing *P*, *sp*-absent reactions (1) and (2) are still proceeding to the right, driving up the alumina content of the *px*, such that the *opx* apex of the *opx+plag+sp+(ol+cpx)* triangle moves continuously down and to the right with increasing *P* (i.e., increasing in Al_2O_3 as the alumina isopleths in *P*-*T* space are crossed, while simultaneously decreasing in Fe_2O_3). This is illustrated schematically in Figures 5b-5f. The precise trajectory of the *opx* apex with increasing *P* for a natural peridotite composition requires the simultaneous solution of the equilibria in reactions (1), (2), and (3) (plus any other independent reactions involving *opx*), which is done implicitly via the energy minimization approaches of the pMELTS and JH-15 calculations.

With still further increases in *P*, the *opx+plag+sp+(ol+cpx)* triangle continues to move to the right, getting progressively narrower along with the *opx+plag+*(*ol+cpx*) and *plag+sp+*(*ol+cpx*) two-phase regions, until anorthite disappears completely from the phase diagrams via the univariant, Fe^{3+}-free end-member version of reaction (3) (i.e., at the right-edge

This is a preprint, the final version is subject to change, of the American Mineralogist (MSA)
Cite as Authors (Year) Title. American Mineralogist, in press.
DOI: https://doi.org/10.2138/am-2020-7162

of the $Si_{½}O$-$Al_{⅔}O$-$Fe_{⅔}O$ plane; Fig. 5g). Although *plag*-out for a Fe^{3+}-bearing lherzolite must occur at a lower *P* than this univariant reaction, the low Fe^{3+} contents of natural peridotites suggest that the *P* difference between *plag*-out (Fig. 5e) and the disappearance of *plag* from the Fe^{3+}-free end member system via this univariant reaction (Fig. 5g) is expected to be small. We determined that based on pMELTS, the difference between *plag*-out in the Cr^{3+}-free DMM composition at the full Fe^{3+} content assumed here for DMM and for a Cr^{3+}- and Fe^{3+}-free DMM equivalent is ~0.3 kbar at 1100°C, consistent with the expectation that this *P* interval is small.

The *P* difference between *sp*-in (Fig. 5c) and *plag*-out (Fig. 5e) is also expected to be small as it reflects to the passage of the narrow *opx+plag+sp+(ol+cpx)* triangle over a bulk composition plotting near the Fe^{3+}-free edge of the model system shown in Figure 5. Based on pMELTS calculations on a Cr^{3+}-free DMM equivalent, the width of this transition is ~1.3 kbar at 1100°C. Similarly, the width of this transition in a Cr^{3+}-free KLB-1 equivalent at 1100°C based on the JH-15 model is ~1.2 kbar (see Fig. 3 in Jennings and Holland, 2015). However, these values are likely upper limits to the width of this interval in the model system of Figure 5 because the width of the transition for a Cr^{3+}- and Fe^{3+}-free DMM equivalent based on pMELTS at 1100°C is still ~0.9 kbar, despite the absence of Cr^{3+} and Fe^{3+}; the persistence of this *P* interval in the Cr^{3+}- and Fe^{3+}-free composition is probably due to effects such as Fe^{2+}-Mg partitioning among the phases (which would not apply to the quinary model system shown in Fig. 5).

Cr_2O_3 and Fe_2O_3 have similar effects on the phase equilibria of peridotite systems in that both are concentrated into *sp* and thus stabilize a *sp* phase, lowering the *P* of *sp*-in and *plag*-out and raising the *P* of *sp*-out (see the section below on the *gt*-lherzolite facies) relative to systems in which they are absent. Indeed, if Figures 5b-5f were drawn with the lower left apex of the compositional triangle being $Cr_{⅔}O$ rather than $Fe_{⅔}O$ and Fe^{3+} were replaced with Cr^{3+} in all the mineral formulae, the sequence of isothermal sections would be topologically similar and could be used to analyze the sequence of assemblages of a Cr^{3+}-bearing peridotite with increasing *P*. However, the concentration of Cr_2O_3 in peridotite is usually much higher than that of Fe_2O_3, so

This is a preprint, the final version is subject to change, of the American Mineralogist (MSA)
Cite as Authors (Year) Title. American Mineralogist, in press.
DOI: https://doi.org/10.2138/am-2020-7162

the bulk composition of the peridotite (i.e., the position of the green dot) would be further to the left and a Cr^{3+}-rich *sp* would be stabilized at much lower *P* than an Fe^{3+}-rich *sp* in a Cr^{3+}-absent system. Given the Cr^{3+} contents of most peridotites, a Cr^{3+}-rich *sp* is typically stable at 1 bar (even in the absence of Fe^{3+}), and their bulk compositions would be in the *opx*+*plag*+*sp*+(*ol*+*cpx*) triangle throughout the *plag*-stability field (Borghini et al., 2009). This is the case for the pMELTS and JH-15 results for the Fe^{3+}+Cr^{3+}-bearing DMM peridotite composition, which predict the presence of Cr^{3+}-rich *sp* all the way down to 1 bar as shown in Figures 3b3 and 3a3 (this would not be the case for the Cr^{3+}-absent, Fe^{3+}-bearing model composition illustrated in Fig. 5). Note that the stabilization of Cr^{3+}-rich *sp* (which is predicted to contain relatively high Fe^{3+} concentration; see Figs. 3a2 and 3b2) outside of the nominal *sp*-lherzolite facies is diminished in the JH-15 model relative to the pMELTS model by the partitioning of both Cr^{3+} and Fe^{3+} into *px* and/or *gt* (hence the difference between *sp* abundances based on pMELTS [Figs. 3a3] and JH-15 [Fig. 3b3], reflecting that pMELTS does not allow Cr^{3+} to go into *px* or *gt* or Fe^{3+} to go into *gt*). Nevertheless, Cr^{3+} is present in sufficient abundance in most peridotites that chromite-rich *sp* is nearly ubiquitous in peridotites at *P*s from 1 bar extending to well into the *gt*-lherzolite facies (Pearson et al., 2003; Warren, 2016).

The way in which the stability of Cr^{3+}-rich *sp* to lower and higher *P*s relative to Cr^{3+}-free systems influences the issues we are interested in here is best illustrated by the JH-15 calculations, in which partitioning of Cr^{3+} into *px* prevents the significant overestimation of *sp* stabilization present in the pMELTS model. Most importantly, the stabilization of Cr^{3+}-rich *sp* means that the activities of other *sp* components – especially $(Mg,Fe)Al_2O_4$ and magnetite – do not have to be high in order for $Al^{3+}$and Fe^{3+} to partition significantly into the *sp* phase. Several features of the results for DMM based on the JH-15 model (Fig. 3) show the onset of significant production of aluminous components in the calculated *sp* in the DMM composition by reactions such as (3) at ~6 kbar: e.g., the simultaneous upswings in *sp*, *opx*, and *cpx* abundances downswings in *plag* and *ol* abundances (Fig. 3b3); the slope-breaks in the progressively decreasing magnetite content (Fig. 3b2) and Cr# (not shown) and progressively increasing Al_2O_3

This is a preprint, the final version is subject to change, of the American Mineralogist (MSA)
Cite as Authors (Year) Title. American Mineralogist, in press.
DOI: https://doi.org/10.2138/am-2020-7162

content (not shown) of the calculated *sp*; and the changing slope of the calculated concentration of Fe^{3+} in the *opx* (Fig. 3b2). Although consumption of *plag* and *ol* with increasing *P* via reactions (1) and (2) and the concomitant decrease in fO_2 due to Fe^{3+} dilution in *px* occur at lower *P* than that at which reaction (3) begins to be significant, the effects of Fe^{3+} dilution on fO_2 (regardless of how – or whether – fO_2 is normalized; see Figs. 2a, 2b, 3a1, and 3b1) are accelerated by the kicking-in of reaction (3) at ~6 kbar, which is in effect analogous to the right edge of the *opx+plag+sp+(ol+cpx)* triangle crossing over the bulk composition in Figures 5c-5e.

As described previously, there will be some redistribution of Fe^{3+} between *sp*, *opx*, and *cpx* with increasing *P*, but these effects are less important in controlling fO_2 than are the effects of dilution – dominantly in the *px* and less so in the *sp* – driven by the volume changes of the continuous solid-solid reactions involving increases in Al-coordination. As explained above, it is this dominant role of *px* as opposed to *sp* in this dilution effect that explains why the calculations of Ballhaus and Frost (1994) and Ballhaus (1995) overestimated the decrease in fO_2 upon conversion of *plag* lherzolite to *sp* lherzolite relative to our results; i.e., most of the Fe^{3+} in the system is in the *px* and this effect occurs whether or not *sp* is stabilized (see the blue curve in Fig. 2d). We also ran pMELTS simulations on a Cr^{3+}-free DMM composition, and although the amounts of *sp* are much lower than in the simulations on the actual Cr^{3+}-bearing DMM composition, the fO_2 trends are similar in both cases, consistent with the conclusion that *sp* is not the principal driver of the modeled trends. Nevertheless, the concentration of the magnetite component in *sp* is still a valuable passive indicator or monitor of fO_2 in peridotites via the reaction $3\ Fe_2SiO_4^{ol} + ½\ O_2 \rightleftharpoons 3\ FeSiO_3^{opx} + Fe_3O_4^{sp}$ given the ubiquity of *ol*+o*px*+*sp* assemblages (e.g., Wood, 1991). This is also true for the approach to modeling fO_2 in peridotites using Fe^{3+}-bearing defects in *ol* developed by Gaetani (2016): although variations in the small amounts of Fe^{3+} in *ol* are unlikely to *control* variations in peridotite fO_2 with *P* and *T*, they might nevertheless be useful passive tracers of peridotite fO_2.

The effects of *P* on fO_2 in the *sp*-lherzolite facies. As described previously, the disappearance of *plag* from the thermodynamically calculated stable assemblage reflects the

This is a preprint, the final version is subject to change, of the American Mineralogist (MSA)
Cite as Authors (Year) Title. American Mineralogist, in press.
DOI: https://doi.org/10.2138/am-2020-7162

sweeping of the *opx*+*plag*+*sp*+(*ol*+*cpx*) triangle to the right in Figure 5 such that, relative to the triangle, the peridotite composition moves from the inside of the triangle (Fig. 5d) to the left of the triangle (i.e., into the *opx*+*sp*+(*ol*+*cpx*) field; Fig. 5f) with increasing *P*. Although *plag* disappears from the assemblage at the *P* of Fig. 5e, as described previously it does not disappear from the isothermal sections until the slightly higher *P* where the selected isotherm crosses the univariant reaction (3) in the Fe^{3+}-absent end-member system (Fig. 5g). The simple topology of Figure 5h then prevails over most of the *sp*-lherzolite facies, until *gt* appears near the upper *P* limit of the *sp*-lherzolite facies (see Figs. 5i and 5j).

As was the case for the *plag*-stability field, we can understand changes in fO_2 with increasing *P* in the *sp*-lherzolite facies by thinking about reactions involving aluminous phases and the *P*-dependent changes in Al-coordination that drive these reactions. A representative reaction in the FeO-$Al_{⅔}$O-$Si_{½}$O system is

⅖ fayalite (*ol*) + ⅗ Fe-Tschermak (*px*)
= ⅖ hercynite (*sp*) + ⅗ ferrosilite (*opx*). (4)

The details of the comparable reaction in the MgO-end-member system have been the subject of much investigation, and there is general agreement that, in *P*-*T* space, alumina isopleths for *px* in the *sp*-lherzolite facies are largely insensitive to *P*, reflecting the fact that the standard-state volume change is close to zero for this reaction (e.g., MacGregor, 2015). This is consistent with the calculated peridotite phase equilibria based on either the pMELTS or JH-15 models; i.e., the modeled abundances of *ol*, *sp*, and *px* are essentially constant across the *sp*-lherzolite facies (Figs. 3a3 and 3b3). As a consequence, the concentrations (Figs. 3a2, 3b2, 2g, and 2h) and activities (Figs. 2e and 2f) of Fe_2O_3 in *px* (and *sp*) in this field also change relatively little, being neither diluted nor concentrated in these phases with changing *P*. For the JH-15 model, this results in an essentially constant fO_2 relative to a metastable *ol*+*opx*+*cpx* assemblage (see the orange curve in Fig. 2b) or slightly increasing ΔFMQ (Fig. 3b1), and for the pMELTS model in a slightly decreasing ΔFMQ (Fig. 3a1); this contrasts with the strongly decreasing fO_2 with *P* in

This is a preprint, the final version is subject to change, of the American Mineralogist (MSA)
Cite as Authors (Year) Title. American Mineralogist, in press.
DOI: https://doi.org/10.2138/am-2020-7162

the *plag*-stability field. The important point is that in both the *sp*- and *plag*-stability fields, the effects of heterogeneous phase equilibria on fO_2 based on these models can be simply understood by examining changes in the amounts of *px*. In the *sp*-lherzolite case, the absence of significant *P* dependence of reaction (4) and the equal amount of *px* on both sides of the reaction mean that the concentrations (and activities) of Fe^{3+}-bearing components in *px* (and in *sp*) are not greatly changed by passive dilution or enrichment as *P* changes across the *sp*-lherzolite facies.

In the context of the schematic phase relations illustrated in Figure 5, the previous paragraph means that the lower boundary of the *opx* field (i.e., the upper termination of the *opx*+*sp*+(*ol*+*cpx*) tie lines at the edge of the red *opx* field) does not move significantly (either up or down) with increasing *P*, and the orientations of the tie lines (i.e., the Fe^{3+}/Al partitioning between *opx* and *sp*) do not change significantly, and thus the Fe^{3+} content of the *opx* in the assemblage is largely unchanged. Note, however, that even if the edge of the *opx* field coexisting with *sp* were moving toward or away from the $Si_{1/2}O$ vertex, the topology of the diagram predicts smaller effects on fO_2 compared to the analysis of the *plag*-lherzolite assemblage (Fig. 6a) because the *opx*-*sp* tie lines are considerably longer than the *opx*-*plag* tie lines (and are not anchored to the Fe^{3+}-free projected anorthite point) and the *opx*/*sp* ratio is significantly higher than the *opx*/*plag* ratio. Thus, the same movement of the edge of the *opx* field toward or away from more aluminous *px* compositions would have less influence on the mole fraction of Fe^{3+} in the *opx* and hence on fO_2 in the *sp*-lherzolite facies than in the *plag*-lherzolite facies.

Variations in fO_2 in the *gt*-lherzolite facies

Graphical analysis of the *gt*-lherzolite facies. The transition from *sp* lherzolite to *gt* lherzolite can also be visualized using the projection shown in Figure 5. Starting from the *sp*-lherzolite facies represented graphically by Figure 5h, we assume *gt* first appears via the univariant reaction ¾ ferrosilite + ¼ hercynite = ¼ fayalite + ¾ almandine in the FeO-$Al_{⅔}O$-$Si_{½}O$ ternary system; this univariant reaction projects onto the $Si_{½}O$-$Al_{⅔}O$ edge of the bounding triangle (Fig. 5i). In reality, it is more likely that *gt* first appears in this MgO-free model

This is a preprint, the final version is subject to change, of the American Mineralogist (MSA)
Cite as Authors (Year) Title. American Mineralogist, in press.
DOI: https://doi.org/10.2138/am-2020-7162

lherzolite system by a univariant reaction among hedenbergite, ferrosilite, hercynite, fayalite, and a binary grossular-almandine *gt* in the CaO-FeO-Al_2O_3-SiO_2 quaternary sub-system (MacGregor, 1967). This univariant reaction would still project along the $Si_{½}O$-$Al_{⅔}O$ edge of the bounding triangle of Figure 5i, but the position of the binary *gt* would be displaced from almandine toward grossular, which in this projection plots farther down towards hercynite (or even beyond it if the *gt* were sufficiently rich in grossular). Although we cannot rule out the first appearance of *gt* as a quinary, Fe^{3+}-bearing *gt*, our assumption that it first stabilizes as an Fe^{3+}-free (or perhaps Fe^{3+}-poor) *gt* in the model system of Figure 5 is consistent with the results of Woodland and O'Neill (1993) and the JH-15 model (Jennings and Holland, 2015). For simplicity, we choose to show the first appearance of *gt* as pure almandine in Figure 5 because including Ca- and/or Fe^{3+}-bearing *gt* end members (such as grossular, andradite, and/or skiagite) would add complexity but no additional graphical insights unless the first-appearing *gt* were significantly more Fe^{3+}-rich than predicted by the JH-15 model.

Increasing *P* beyond the univariant appearance of almandine in the Fe^{3+}-free model system produces a configuration such as that shown in Figure 5j, with a three-phase *opx*+*sp*+*gt*+(*ol*+*cpx*) triangle sweeping across the diagram to the left, opening up (1) a two-phase *gt*-lherzolite facies with the assemblage *opx*+*gt*+(*ol*+*cpx*) for more *opx*-rich compositions plotting above almandine and to the right of the *opx*+*gt*+(*ol*+*cpx*) edge of the triangle, and (2) a second two-phase region, *gt*+*sp*+(*ol*+*cpx*), below almandine and to the right of *gt*+*sp*+(*ol*+*cpx*) edge of the triangle. The triangle is initially narrow and close to the projected $Si_{½}O$-$Al_{⅔}O$ join, so at the *P* of Figure 5j, the peridotite composition (shown by the green symbol) is still in the *sp*-lherzolite facies (i.e., it is in the two-phase *opx*+*sp*+(*ol*+*cpx*) field covering most of the diagram). As described above, we assume that *gt* first appears as a stable phase at pure almandine. However, with increasing *P*, *gt* is assumed to be a binary solid solution extending from almandine towards skiagite. This solid solution is shown in each panel after Fig. 5i as a red horizontal line, the Fe^{3+}-rich end of which extends progressively further toward skiagite with increasing *P*, reflecting the increasing stability

This is a preprint, the final version is subject to change, of the American Mineralogist (MSA)
Cite as Authors (Year) Title. American Mineralogist, in press.
DOI: https://doi.org/10.2138/am-2020-7162

of Fe^{3+}-bearing *gt* at higher *P* (e.g., O'Neill et al., 1993; Woodland and O'Neill, 1993; Rohrbach et al., 2007; Stagno and Frost, 2010; Jennings and Holland, 2015).

With increasing *P*, the *opx*+*sp*+*gt*+(*ol* +*cpx*) triangle continues moving to the left (i.e., the field of *gt* stability expands), and at the *P* shown in Figure 5k, the left (i.e., the *opx*+*sp*+(*ol* +*cpx*)) edge of the triangle has reached the green symbol, corresponding to *gt*-in. Beyond this point, *gt* joins the assemblage, as with further increase in *P*, the left edge of the triangle passes over the bulk composition, after which the green symbol plots within the triangle (Fig. 5l) and the phase assemblage is *opx*+*sp*+*gt*+(*ol* +*cpx*), corresponding to a *sp*+*gt* lherzolite. Note that the *P* of the *gt*-in reaction depends on the Fe^{3+} content of the bulk composition; it is always at higher *P* than the univariant reaction in the end-member Fe^{3+}-free system (Fig. 5i), and the difference increases for lherzolites with higher Fe^{3+} contents, as demonstrated by MacGregor (1970). However, just as was shown above that in the absence of Cr^{3+} there is only a small *P* difference between the *P*s of *sp*-in, *plag*-out, and the *plag*→*sp* univariant reaction in the Fe^{3+}-free subsystem in a low-Fe^{3+} composition such as DMM, the *P* difference between the appearance of *gt* in the Fe^{3+}-free end-member system and in a low-Fe^{3+} lherzolite is expected to be small. Based on pMELTS calculations at 1100°C, the *P* difference between the univariant *gt*-in reaction in a Cr^{3+}- and Fe^{3+}-free DMM equivalent and *gt*-in in a Cr^{3+}-free composition that has the full complement of Fe^{3+} of our model DMM composition is 0.8 kbar, consistent with this expectation.

With still further increases in *P*, the *opx*+*sp*+*gt*+(*ol* +*cpx*) triangle moves far enough to the left that the upper right edge of the triangle (i.e., the *opx*+*gt*+(*ol*+*cpx*) edge) reaches the bulk composition (Fig. 5m), and the amount of *sp* in the assemblage is zero at this point, corresponding to *sp*-out. At higher *P*, the bulk composition is in the *opx*+*gt*+(*ol*+*cpx*) two-phase region (Fig. 5n), and the peridotite is a *gt* lherzolite. The *P* where *sp*-out occurs clearly depends both on the bulk composition of the peridotite (i.e., it would be higher for higher Fe^{3+} contents because the triangle would have to move further to the left for higher Fe^{3+} contents in order for the composition no longer to fall within the triangle) and on the Fe^{3+} content of the *gt* apex of the

This is a preprint, the final version is subject to change, of the American Mineralogist (MSA)
Cite as Authors (Year) Title. American Mineralogist, in press.
DOI: https://doi.org/10.2138/am-2020-7162

triangle (i.e., if the *gt* were assumed to be Fe^{3+}-free, the upper-right edge of the triangle would cross over the peridotite bulk composition at higher *P* than if, as depicted in Figure 5m, the *gt* contains Fe^{3+}). Moreover, as described previously for the *plag*→*sp*-lherzolite transition, addition of Cr^{3+} to the system has effects similar to (and, due its higher concentration, larger than) those of Fe^{3+} in broadening the *P* interval over which the *sp*→*gt*-lherzolite transition occurs (O'Neill, 1981; Nickel, 1986). Cr^{3+}, like Fe^{3+}, increases the *P* of both *gt*-in and *sp*-out, with a larger effect on *sp*-out (Jennings and Holland, 2015). As mentioned previously in connection with the *plag*→*sp*-lherzolite transition, this could be understood qualitatively with diagrams comparable to those of Figure 5 but in which $Fe_{⅔}O$ is replaced by $Cr_{⅔}O$. Note again, however, that *sp* only disappears from the assemblage if and when the Cr^{3+} content is fully accommodated in *px*+*gt*; this never occurs in pMELTS because the only subsolidus host for Cr^{3+} in this model is *sp*.

The sequence of phase assemblages with increasing *P* illustrated by the model isothermal sections shown in Figures 5h-5n corresponds well to the thermodynamically calculated sequence of phase assemblages shown in Figures 3a3 and 3b3 and to experimental results (e.g., O'Neill, 1981; Nickel, 1986; Robinson and Wood, 1998). Focusing on the JH-15 calculations, as *P* increases from the *sp*-lherzolite facies (Fig. 5h), *gt* appears as the left edge of the *opx*+*sp*+*gt*+(*ol* +*cpx*) triangle moves from right to left over the bulk composition (Figs. 5j→5k). As *P* increases and the triangle continues to move to the left, both the abundance and Fe^{3+} content of *gt* increase while the abundance of *sp* decreases and its Fe^{3+} content increases over a narrow *P* range until *sp* is exhausted when the right edge of the triangle coincides with the bulk composition (Fig. 5m; Figs. 3b3 and 3b2). The narrow *P* range of *sp*+*gt* lherzolite stability in DMM based on JH-15 (0.5-0.6 kbar; Fig. 3b3) reflects the narrowness of the *opx*+*sp*+*gt*+(*ol* +*cpx*) triangle in Figure 5k-5m, due its nearness to the Fe^{3+}-free edge of the diagram (because of the low Fe^{3+} and Cr^{3+} contents in the DMM composition); to the fact that this model bulk composition (like most natural peridotites) plots near the *opx* apex of the three-phase triangle (where the triangle is narrowest) because *opx* is significantly more abundant than *gt* in the relevant *P* range; and to the capacity of *gt* to dissolve significant Cr^{3+}. Note that the calculated width of this transition based

This is a preprint, the final version is subject to change, of the American Mineralogist (MSA)
Cite as Authors (Year) Title. American Mineralogist, in press.
DOI: https://doi.org/10.2138/am-2020-7162

on JH-15 is similar (0.3-0.4 kbar) to that of the fertile KLB-1 composition (Jennings and Holland, 2015). The overall sequence of phase assemblages is similar for the pMELTS calculation, although again *sp* never disappears from the Cr^{3+}-bearing assemblage in this case (i.e., the bulk composition never exits the *opx*+*sp*+*gt*+(*ol* +*cpx*) triangle).

The sequence of phase assemblages in a representative peridotite composition with increasing *P* described in the previous paragraphs is associated with a progressive increase in fO_2 relative to FMQ or to a metastable *ol*+*opx*+*cpx*±*sp* assemblage of as much as 1-1.5 orders of magnitude from *gt*-in up to ~30 kbar (Figs. 3a1, 3b1, 2a, 2b). That this increase in normalized fO_2 is related primarily to stabilization of *gt* was demonstrated previously using the results of the metastable calculations shown in Figure 2. In particular, using either pMELTS (Fig. 2c) or JH-15 (Fig. 2d), the discontinuous increase in the slope of the fO_2 vs. *P* trend at *gt*-in and the downward curvature of the fO_2 vs. *P* curve in the *gt* stability field are only present when *gt* is allowed to appear in the assemblage. Although they differ in detail, that the pMELTS (Figs. 2a vs. 2c) and JH-15 (Figs. 2b vs. 2d) models both produce similar results for the effects of *gt* on fO_2 normalized to a metastable *ol*+*opx*+*cpx*±*sp* assemblage demonstrates that the connection between increasing fO_2 and the production of *gt* over the *P* range we have modeled does not depend strongly on the treatment of Fe^{3+} and Cr^{3+} in *gt* or *px* or on other differences between the two thermodynamic models.

Coupling between alumina in *px* and fO_2 in the *gt*-lherzolite facies. The increase in fO_2 relative to metastable *ol*+*opx*+*cpx*±*sp* assemblages that results from *gt* stabilization with increasing *P* is the reverse of the effect of *plag* destabilization described previously. Figures 2c and 2d show that fO_2 increases in going from a metastable *gt*-absent assemblage in the pMELTS calculation or a metastable *gt*+*sp*-absent assemblage for the JH-15 calculation to a more stable *gt*-bearing assemblage (e.g., from the horizontal lines at zero to the elevated purple curves above ~20 kbar in Fig. 2c and ~14.5 kbar in Fig. 2d). In the pMELTS model, *gt* forms from the metastable, *gt*-free assemblage by reactions between *sp* and *px* such as

This is a preprint, the final version is subject to change, of the American Mineralogist (MSA)
Cite as Authors (Year) Title. American Mineralogist, in press.
DOI: https://doi.org/10.2138/am-2020-7162

¼ hercynite (*sp*) + ¾ ferrosilite (*opx*) = ¾ almandine (*gt*) + ¼ fayalite (*ol*), (5)

and by reactions between *px* components alone (i.e., without *sp*) such as

½ Mg-Tschermak (*px*) + ½ enstatite (*px*) = pyrope (*gt*), (6a)

or the equivalent for the model Fe^{2+}-end-member system shown in Figure 5,

½ Fe-Tschermak (*px*) + ½ ferrosilite (*px*) = almandine (*gt*). (6b)

For the JH-15 model, only reactions (6a) and (6b) apply because *sp* is not present in the metastable reference assemblage or in the stable assemblage in Figure 2d. Similar *px*-consuming reactions that generate grossular-bearing *gt* can be written with Ca-Tschermak, hedenbergite, or diopside *px* components. Reactions (5) and (6) show that formation of one mole of *gt* consumes one mole of *px* (on a single oxygen basis). Based on either model, for an isobaric, isothermal transformation from the metastable *gt*-absent to the *gt*-bearing assemblages, the decrease in the amount of *px* (and *sp* in the pMELTS calculations) results in increases in the concentrations (and activities) of their Fe^{3+}-bearing components and therefore in the fO_2. As described and emphasized above for the case of *plag* consumption via reaction with *ol* (such as reactions [1] and [2]), this effect is primarily a passive one, driven by redistribution of Al towards the more stable (and lower molar volume components) on the right-hand sides of reactions (5) and (6) rather than to reactions involving Fe^{3+} *per se*. However, the concave down trend in fO_2 with *P* relative to the metastable *ol*+*opx*+*cpx*±*sp* assemblage reaches a maximum for the JH-15 model at ~30 kbar, and as described below, we attribute this primarily to the effects of redistribution of Fe^{3+} between *px* and *gt* due to the progressively increasing amount of Fe^{3+} in *gt* relative to *px* with increasing *P* in the *gt*-lherzolite field: i.e., the fraction of Fe^{3+} in the stable system that is in *gt* as opposed to *px* increases from ~6% at *sp*-out to almost 50% at 40 kbar. Note that the concave down shape of $\log_{10} fO_2$ (normalized to a metastable *gt*-free assemblage) vs. *P* is present in the pMELTS calculations (including for a Cr^{3+}-free composition, which avoids artifacts due to the overstabilization of *sp*), which do not include any Fe^{3+} in the *gt*. Thus, although likely

This is a preprint, the final version is subject to change, of the American Mineralogist (MSA)
Cite as Authors (Year) Title. American Mineralogist, in press.
DOI: https://doi.org/10.2138/am-2020-7162

amplified in the JH-15 model due to progressive partitioning of Fe^{3+} into *gt* with increasing *P*, this feature probably also reflects the progressively diminishing effectiveness of reactions (6a) and (6b) at increasing the modal abundance of *gt* at the expense of *px* with increasing *P*, which in turn diminishes the effect of concentration of Fe^{3+} with progressive *gt* formation; this is consistent with the concave down trend of *gt* abundance and concave up trends in *opx* and *cpx* abundances shown in Figs. 3a3 and 3b3. Note also that for the JH-15 calculation, allowing *sp* to be stable in the initial metastable assemblage has only a minor effect on its fO_2 (i.e., compare the orange curve with the horizontal line in Fig. 2d), so these same statements apply to conversion of a metastable *sp* lherzolite to the more stable assemblage in which *gt* is the only stable high-Al phase.

The analysis of the previous paragraph focuses on the role of *gt* formation without considering the interaction between *sp* and *gt* in their overlapping stability fields. The transition from *sp* lherzolite to *gt* lherzolite over a small *P* range was anticipated in our discussion of Figures 5j-5n earlier in this section, reflecting the narrow interval of increasing *P* required for passage of the *opx*+*gt*+*sp*+(*ol*+*cpx*) triangle over the peridotite composition. The importance of this 0.5-0.6 kbar *P* interval between *gt*-in and *sp*-out in the JH-15 model (Fig. 3b3) is manifested in Figures 2b and 3b1 by the steep ~0.5 log unit increase in both absolute and normalized (either ΔFMQ or relative to a metastable *ol*+*opx*+*cpx* assemblage) fO_2 over this *P* interval. Significantly, this increase in fO_2 is accompanied by a large increase in *gt* abundance from 0 to ~10 wt. % while *opx* abundance decreases by ~30% (from ~27 to 19%) and *cpx* abundance decreases by ~15% (from ~15 to 13%).

The leftward movement of the *opx*+*gt*+*sp*+(*ol*+*cpx*) triangle across the model peridotite composition with increasing *P* (Figs. 5k-5m) can be understood via the stoichiometry of reaction (5) or by a comparable reaction involving consumption of Ca-bearing pyroxene components. Thus, as with the *sp*-absent reactions (6a) and (6b), for every mole of *gt* generated, one mole of *px* is consumed. Again, because most of the Fe^{3+} in the system is in *px* both before and after the *sp*→*gt*-lherzolite transition (especially for the JH-15 calculations; Figs. 4b and 4d), the

This is a preprint, the final version is subject to change, of the American Mineralogist (MSA)
Cite as Authors (Year) Title. American Mineralogist, in press.
DOI: https://doi.org/10.2138/am-2020-7162

consumption of Fe^{3+}-free *px* components by reaction (5) leads to increases in the concentrations and activities of Fe_2O_3 in the residual *opx and cpx* and a concomitant increase in fO_2 over the narrow *P* interval in which *sp* and *gt* coexist in the JH-15 model (Figs. 3b1-3b3). This effect is also qualitatively understandable graphically by comparing Figure 5j (just below *gt*-in) and Figure 5n (just above *sp*-out): The tie-line between *opx* and *sp* is much longer in Figure 5j than the tie-line between *opx* and *gt* in Figure 5n, and thus for the same bulk composition (the green symbol), the abundance of *opx* in the assemblage is lower in the *gt*-lherzolite facies than in the *sp*-lherzolite facies, leading to concentration of Fe^{3+} in the *opx* and therefore to higher fO_2 in the *gt*-lherzolite assemblage relative to the *sp*-lherzolite assemblage; note that such quantitative features can be misleading in projections such as that used in Figure 5, but the substantial decreases in *opx* abundance inferred with decreasing *P* graphically accompanying the *sp*→*gt*-lherzolite transition is confirmed by the JH-15 calculations (both for *opx* and *cpx*; Fig. 3b3).

Simultaneous with reaction (5) being driven to the right with increasing *P*, the right-hand sides of reactions (6a) and (6b) are also favored with increasing *P*. Thus, if we only looked at reaction (5), one might conclude that with its consumption of the ferrosilite component of the *opx*, it would lead to a passive increase in the concentration in the *opx* of Al_2O_3 (i.e., in the concentration of the Fe-Tschermak component) as well as of Fe_2O_3 (which leads to the large increase in fO_2 across the narrow *sp*→*gt*-lherzolite transition). However, this is counteracted by the consumption of the Fe-Tschermak component via reaction (6b) as the transition from *sp*→*gt* lherzolite is crossed with increasing *P*, such that the Al_2O_3 concentration of the *opx* is little changed over this small *P* interval (Fig. 2h). Graphically, this means that the *opx* apex of the *opx*+*gt*+*sp*+(*ol*+*cpx*) triangle moves little over the small *P* interval between Figure 5k and 5m. As described above for the comparable discussion for the *plag*→*sp*-lherzolite transition, the details of the trajectory of the *opx* apex across the *sp*→*gt*-lherzolite transition requires simultaneous solution of the equilibria in reactions (5) and (6) and other independent reactions among the phases and components in the system, and therefore cannot be fully evaluated by focusing on one reaction alone.

This is a preprint, the final version is subject to change, of the American Mineralogist (MSA)
Cite as Authors (Year) Title. American Mineralogist, in press.
DOI: https://doi.org/10.2138/am-2020-7162

Although the same increases in absolute and normalized fO_2 with *P* just above *gt*-in seen in the JH-15 calculation are present in the pMELTS calculation (Figs. 2a and 3a1), they are more gradual because the treatment of Cr^{3+} in pMELTS widens the *P* interval over which most of the hercynite transfers into *gt*. Note that because at least some *sp* is always present in the pMELTS calculations (albeit at low abundances beyond the transitional region above *gt*-in; Fig. 3a3), the increases in fO_2 with *P* resulting from reactions (5) and (6) are accompanied by a substantial progressive increase in the concentration (Fig. 3a2) and activity of the magnetite component in the residual *sp*. This is shown in Figures 5k-5n by the progressive leftward movement of the *sp* corner of the *opx*+*sp*+*gt*+(*ol*+*cpx*) triangle with increasing *P*. Although as described previously for the region of *sp*+*plag* coexistence, *opx* and *cpx* still contain more than 50% of the Fe^{3+} in the system in the pMELTS calculations (Fig. 4a), *sp* contains the remainder of the Fe^{3+} in the system and is a major reservoir for Fe^{3+}. Nevertheless, the overall similar shapes and magnitudes of fO_2 variations in the pMELTS and JH-15 models as the *gt* field is traversed with increasing *P* suggests that this artifact of the pMELTS model does not exert significant control over the fO_2 variations correlated with the phase changes involving aluminous phases on which we have focused. Note that we also ran the pMELTS calculations on a Cr^{3+}-free DMM composition; in this case, just as it does for the Cr^{3+}-bearing JH-15 model, *sp* disappears from the phase assemblage at a *P* just above *gt*-in, and fO_2 relative to a metastable *ol*+*opx*+*cpx*+*sp* assemblage increases steeply in this zone reflecting the passage of the narrow *opx*+*sp*+*gt*+(*ol*+*cpx*) triangle over the Cr^{3+}-free composition; i.e., when the artifact of the pMELTS modeling always stabilizing *sp* is removed, this difference between the pMELTS and JH-15 models in the low-*P* region of the *gt*-lherzolite facies is no longer present.

The effect of Fe^{3+} in *gt*. To this point, we have emphasized the importance of passive dilution or enrichment of Fe^{3+} in the dominant Fe^{3+}-bearing phases (*opx* + *cpx*) that accompanies their production or consumption as a result of heterogeneous equilibria to explain the changes in fO_2 relative to metastable *ol*+*opx*+*cpx*±*sp* assemblages that are observed in our models. As described previously, however, redistribution of Fe^{3+} between phases does occur, and can also

This is a preprint, the final version is subject to change, of the American Mineralogist (MSA)
Cite as Authors (Year) Title. American Mineralogist, in press.
DOI: https://doi.org/10.2138/am-2020-7162

play a role. The most important example of this in our modeling is the progressive transfer of Fe^{3+} from *px* to *gt* from *gt*-in up to 40 kbar based on the JH-15 calculations; the results of Jennings and Holland (2015) suggests this trend continues to at least 60 kbar. The concentration of *gt* in Fe^{3+} relative to *px* with increasing *P* is well known and related to equilibria such as 2 fayalite + ferrosilite + ½ O_2 = skiagite, where the right-hand side is strongly favored by increasing *P* (e.g., Wood et al., 1990; Woodland and O'Neill, 1993; Ballhaus, 1995; Gudmundsson and Wood, 1995; Rohrbach et al., 2007; Frost and McCammon, 2008; Stagno and Frost, 2010). In the output of the JH-15 model, this is manifested by the continuously increasing Fe^{3+} content of the *gt* with increasing *P* at 1100°C starting from its appearance at *gt*-in (see the purple curve in Fig. 3b2) and the decreasing Fe^{3+} concentration in the *opx* above ~18 kbar and in the *cpx* above ~23 kbar (Fig. 3b2): Starting from *gt*-in at ~15 kbar, with increasing *P* up to 40 kbar, $D(Fe^{3+})_{gt/opx}$ (i.e., $Fe^{3+}_{gt}/Fe^{3+}_{opx}$) increases from 0.18 to 1.8, and $D(Fe^{3+})_{gt/cpx}$ increases from 0.48 to 2.6. Thus, with increasing *P* in the *gt*-lherzolite facies, there is a competition between tendency to concentrate Fe^{3+} in the *px* via reactions (5) and (6) — although as mentioned previously this effect diminishes continuously above *sp*-out for the JH-15 model (Fig. 3b3) and above *gt*-in for the pMELTS model (Fig. 3a3) — and the transfer of Fe^{3+} from *px* to *gt* due to the progressive increases in $D(Fe^{3+})_{gt/opx}$ and $D(Fe^{3+})_{gt/cpx}$. The passive concentration of Fe^{3+} in *px* dominates close to *gt* -in, but the partitioning of Fe^{3+} into *gt* becomes progressively more important with increasing *P*, and we speculate that this results in the broad maximum in fO_2 at ~30 kbar when normalized to a metastable *ol*+*opx*+*cpx* assemblage (Fig. 2b); this maximum is also present for ΔFMQ but not in absolute fO_2 (Fig. 3b1). This explanation for the decrease in fO_2 relative to a metastable *gt*+*sp*-absent assemblage at $P \gtrsim 30$ kbar is closely related to that proposed by Ballhaus and Frost (1994) and Ballhaus (1995), although for reasons explained below, their expectation that fO_2 would decrease immediately above *gt*-in is inconsistent with our modeling.

We have not extended our modeling above 40 kbar, but the isothermal decrease in ΔFMQ predicted here above ~30 kbar (Fig. 3b1) is also predicted by the JH-15 model to extend on

This is a preprint, the final version is subject to change, of the American Mineralogist (MSA)
Cite as Authors (Year) Title. American Mineralogist, in press.
DOI: https://doi.org/10.2138/am-2020-7162

isotherms to 60 kbar for the fertile KLB-1 peridotite (Jennings and Holland, 2015) and on a geotherm up to 70 kbar for the moderately depleted Y-17 peridotite (Miller et al., 2016). The continuation of this trend in ΔFMQ to these high *P*s may be due in part to continued transfer of Fe^{3+} into *gt* (especially in the lower *P* part of the 40-70 kbar interval), but the difference in the standard-state volume changes of the FMQ and skiagite-formation reactions also contribute to this effect when the fO_2 is reported as ΔFMQ (Frost and McCammon, 2008).

The pMELTS calculation does not have a maximum in fO_2 relative to a metastable *gt*-absent assemblage in the *gt*-lherzolite field (Fig. 2a). Because pMELTS does not partition any Fe^{3+} into *gt*, the absence of this feature in the pMELTS results is consistent with our explanation that this maximum in the JH-15 results relates to the transfer of Fe^{3+} from *px* to *gt* with increasing *P*. Note, however, that the pMELTS calculations do generate a maximum in ΔFMQ in the *gt* field at about 20 kbar (Fig. 3a1) — consequently, the progressive divergence with increasing *P* above 20 kbar between the FMQ buffer curve (dashed, black) and the absolute fO_2 curve for DMM (solid, black) based on the pMELTS calculations (Fig. 3a1) that results in this maximum in ΔFMQ (the red, solid curve) must reflect other factors.

The decrease in fO_2 relative to a metastable *gt*+*sp*-free assemblage above ~30 kbar for the DMM peridotite composition based on JH-15 is small, and the details depend on many factors embedded in the JH-15 thermodynamic model, including the variations in activity coefficients of the various components for each phase with increasing *P* due changing phase compositions and the balance among products and reactants involving many independent heterogeneous equilibria, each shifting with *P* (and *T*) based on its changing standard-state free energy change. All of these factors are dealt with implicitly in both the pMELTS and JH-15 models, but interpreting the output in terms of which factors dominate is not always straightforward when the factors are pulling in different directions. Nevertheless, we think this is probably a robust result. Supporting this is the observation that the broad maximum in fO_2 relative to a metastable *gt*+*sp*-free assemblage at about 30 kbar is straddled by the *P*s at which Fe^{3+} becomes compatible in *gt* relative to *opx* and *cpx* (i.e., $D[Fe^{3+}]_{gt/opx}$ and $D[Fe^{3+}]_{gt/cpx}$ first exceed 1.0 at 33 and 26 kbar,

This is a preprint, the final version is subject to change, of the American Mineralogist (MSA)
Cite as Authors (Year) Title. American Mineralogist, in press.
DOI: https://doi.org/10.2138/am-2020-7162

respectively), because this is a rough indicator of where the consequences of Fe^{3+} in *gt* will begin to dominate.

We can put the effects of progressive partitioning of Fe^{3+} into *gt* relative to *px* into a graphical context using the projections shown in Figures 5 and 6. With increasing *P* in the *gt*-lherzolite facies (i.e., above *sp*-out, represented by Fig. 5n), the concentration of Fe^{3+} in *opx* for the DMM composition based on JH-15 initially increases. Under these conditions this change in Fe^{3+} in *opx* can be illustrated using Figure 6b, an enlargement of the region around the *gt*-lherzolite facies (i.e., the *gt*+*opx*+(*ol*+*cpx*) field in Fig. 5n). Based on the JH-15 model, at *sp*-out, $D(Fe^{3+})_{gt/opx}$ and $D(Fe^{3+})_{gt/cpx}$ are ~0.2 and 0.5, and $D(Fe^{3+}/Al)_{gt/opx}$ is ~0.06. Based on this partitioning of Fe^{3+} into *px* relative to *gt* (and the strong Fe^{3+}/Al partitioning, which affects tie-line slopes in Figs. 5 and 6), we show in Figure 6b a graphical treatment that approximates the *gt* as Fe^{3+}-free near the low-*P* limit of *gt* stability. This assumption that the *gt* is Fe^{3+}-free maximizes the effects of reactions (6a) and (6b), and it applies exactly to a Cr^{3+}-free pMELTS calculations (which neither overstabilize *sp* due to the treatment of Cr^{3+}, nor places any Fe^{3+} in the *gt*). At low *P* (i.e., just above *sp*-out) the *opx* coexisting with *gt*+(*ol*+*cpx*) plots at point *c* at the upper end of the tie line from *gt* to *opx* that passes through the bulk composition (shown as a green dot). As *P* increases, the *opx* coexisting with *gt*+(*ol*+*cpx*) becomes less abundant and poorer in Al due to reactions (6a) and (6b) proceeding to the right. This is represented in Figure 6b by point *d*, which is on the edge of the *opx* phase field where it intersects with the extension to higher ratios of ferrosilite to the Fe-Tschermak-component of the tie line between almandine and point *c* that passes through the peridotite composition (shown as the green dot); this follows from the fact that neither the peridotite composition nor the composition of the Fe^{3+}-free *gt* (neglecting grossular) have changed, so the *opx* must lie on the same tie line at low and high *P* given the approximation in this construction that the *gt* is Fe^{3+}-free. The movement of the *opx* to lower Al contents with increasing *P* at constant *T* reflects the well-known configuration in *P*-*T* space of alumina isopleths in *opx* in the *gt*-lherzolite facies that results from reactions (6a) and (6b). The main result of this simple graphical construction is that the higher *P opx* (point *d*) has

This is a preprint, the final version is subject to change, of the American Mineralogist (MSA)
Cite as Authors (Year) Title. American Mineralogist, in press.
DOI: https://doi.org/10.2138/am-2020-7162

higher a higher Fe^{3+} content than the lower *P opx* (point *c*) based on the *c*→*d* trajectory across the dotted black lines of roughly constant Fe^{3+} content. The effect of *gt* formation on the concentration of Fe^{3+} in *opx* as *P* increases illustrated in Figure 6b is the reverse of the effect of *plag* consumption with increasing *P* shown in Figure 6a, and in both cases, the increase in the concentrations of Fe^{3+} components in the *px* – whether going down *P* in the *plag*-lherzolite facies or up *P* in the *gt*-lherzolite facies – will generally result in a concomitant increase in fO_2 relative to a metastable *ol*+*opx*+*cpx*± *sp* assemblage (Fig. 2a and 2b). The progressive increase in *gt* abundance at the expense of the *px* with increasing *P* in the *gt*-lherzolite facies present in both the JH-15 and pMELTS models (Figs. 3a3 and 3b3) is also illustrated graphically in Figure 6b by the position of the bulk composition relative to the lengthening *gt*+*opx*+(*ol*+*cpx*) tie line.

As described above for *plag* lherzolites, Figure 6b also demonstrates graphically why transformation at constant *P* and *T* from a metastable *gt*-free assemblage to the stable *gt*-bearing assemblage leads to an increase in fO_2 relative to the metastable assemblage (Figs. 2a-2d). The only aluminous phase in the metastable *ol*+*opx*+*cpx* assemblage that appears in the projection shown in Figure 6b is *opx*. The *opx* in the metastable assemblage must therefore in projection coincide with the bulk composition of the peridotite; i.e., both plot at the position of the green dot. When the metastable assemblage transforms to the stable, *gt*-bearing assemblage, the green dot representing the bulk composition of the peridotite must lie on a stable *opx*+*gt*+*(ol*+*cpx)* tie line at the *P* and *T* of the transformation. Provided that the *gt* is Fe^{3+}-poor, the *opx* composition at the end of a stable *opx*+*gt* tie line passing through the green dot must have higher Fe^{3+} concentrations than the metastable *opx* plotting at the green dot, and hence the fO_2 of the stable assemblage will generally be higher than that of the metastable assemblage (although as described in the next paragraph, this result could change if the *gt* were sufficiently Fe^{3+}-rich).

Figure 6c illustrates a more realistic situation for the high-*P* end of the range we have considered and in which the transfer of Fe^{3+} from *px* into *gt* is inferred to have an effect on fO_2; e.g., by 40 kbar, $D(Fe^{3+})_{gt/opx}$ and $D(Fe^{3+})_{gt/cpx}$ have increased to ~1.8 and 2.6, and $D(Fe^{3+}/Al)_{gt/opx}$ has increased to ~0.13. As in Figure 5, the *gt* now includes significant solid solution from

This is a preprint, the final version is subject to change, of the American Mineralogist (MSA)
Cite as Authors (Year) Title. American Mineralogist, in press.
DOI: https://doi.org/10.2138/am-2020-7162

almandine toward the skiagite end member shown as a red horizontal line (labeled "gt ss" in Fig. 6c). The red edges of the *opx* field are shown schematically for three *P*s. The three black dotted lines are lines of roughly constant projected $Fe_{⅔}O$ content, comparable to those shown in Figures 6a and 6b. Three schematic tie lines are shown, extending from *gt* compositions *1*, *2*, and *3* to *opx* compositions *e*, *f*, and *g*, respectively, with *P* increasing in this tie-line sequence from the low *P* limit of the *gt* stability field up to a *P* above the fO_2 maximum shown in Figures 2b and 2d. The key feature of this exaggerated construction is that the Fe^{3+} content of the *gt* increases from essentially zero for the *1*-*e* tie line to a significant amount for the higher-*P* *3*-*g* tie line. When coupled with the upward movement of the edge of the *opx* field upward with increasing *P* in Figure 6c and with the requirement that each tie line must pass through the bulk peridotite composition (i.e., the green dot in Fig. 6c), this leads to a progressive clockwise rotation of the tie lines (corresponding to an increase with increasing *P* in $D[Fe^{3+}]_{gt/opx}$ from <1 for the *1*-*e* and *2*-*f* tie lines to >1 for the *3*-*g* tie line). This rotation of the tie lines generates the $e \rightarrow f \rightarrow g$ sequence of *opx* compositions. Although the details will depend on the interplay between the rotation of the tie lines and the movement of the edge of the *opx* field with *P*, for the schematic example given in Figure 6b, this leads initially to an increase in the concentration of Fe^{3+} in the *opx* with increasing *P* (from *e* to *f*) followed by a decrease with a further increase in *P* (from *f* to *g*): To the degree that the Fe^{3+} content of the pyroxene correlates positively with the activity of Fe_2O_3, which in turn correlates positively with fO_2 relative to the metastable *gt*+*sp*-free assemblage, the schematic sequence shown graphically in Figure 6c predicts that with increasing *P*, fO_2 relative to the metastable *gt*+*sp*-free assemblage will initially increase, reach a maximum, and then decrease. Although oversimplified, this graphical treatment can rationalize our preferred explanation of the fO_2 maximum in the *gt*-lherzolite field observed in the output of the JH-15 model when fO_2 is given relative to a metastable *ol*+*opx*+*cpx* assemblage (Figs. 2b and 2d) as due to the balance between the retreat of the edge of the *opx* field and the increase in the Fe^{3+} content of the *gt* with increasing *P*.

This is a preprint, the final version is subject to change, of the American Mineralogist (MSA)
Cite as Authors (Year) Title. American Mineralogist, in press.
DOI: https://doi.org/10.2138/am-2020-7162

In summary, we infer that the small (~10%) decrease in $\log_{10} fO_2$ relative to a metastable *ol*+*opx*+*cpx* assemblage that JH-15 predicts from ~30 to 40 kbar is real and not an artifact, and the discussion in this section demonstrates that it can be rationalized by considering the increasing Fe^{3+} contents of the *gt* in the model at this range of *P*s. Nevertheless, this effect is small relative to the overall effects of *gt* formation on fO_2: The main result based on the JH-15 model, as illustrated in Figures 2b and 2d, is that the progressive formation of *gt* primarily via reaction (5) in the narrow *P* interval between *gt*-in and *sp*-out and then via reactions (6a) and (6b) up to ~30 kbar is accompanied by an increase in fO_2 of ~1 order of magnitude relative to a metastable *gt*±*sp*-free assemblage; most of the progressive increase in fO_2 from *gt*-in to ~30 kbar develops nearest the *gt*-in boundary, where the Fe^{3+} content of the *gt* is small relative to that of the *opx* + *cpx*. Moreover, the pMELTS model, which does not include any Fe^{3+} in the *gt* shows essentially the same behavior with a similar magnitude increase in fO_2 as the JH-15 model (compare the panels on the left side of Figure 2 to those on the right), and the correspondence with the JH-15 model is even better if the pMELTS calculation is done on a Cr^{3+}-free equivalent of the peridotite bulk composition (i.e., it has the same narrow transition interval with *sp*+*gt*-bearing assemblages with a steep increase in fO_2 with *P*). That the two models are so similar even though the pMELTS model excludes Fe^{3+} from *gt* is a strong indication that the 1st-order effects are not overwhelmed by the incorporation of Fe^{3+} into *gt* in this *P* range, even though this effect appears to result in a noticeable perturbation in the results of the JH-15 model at the high-*P* end of the calculations we have done.

Comparison to previous work (*gt*-bearing assemblages). In addition to their analysis described above of the change in fO_2 that would accompany the conversion of *plag* lherzolite to *sp* lherzolite, Ballhaus and Frost (1994) and Ballhaus (1995) developed a related analysis to predict changes in fO_2 that result from the conversion of *sp* lherzolite to *gt* lherzolite. They modeled the step-wise conversion of a fertile *sp* lherzolite to a *gt* lherzolite at 25 kbar and 1280°C via *sp* + *px* = *ol* + *gt* reactions (e.g., reaction [5]), and they assumed that when both *gt* and *sp* are present, Fe^{3+} is, at most, weakly partitioned into the *sp* (i.e., $D[Fe^{3+}]_{gt/sp} = Fe^{3+}_{gt}/Fe^{3+}_{sp}$

This is a preprint, the final version is subject to change, of the American Mineralogist (MSA)
Cite as Authors (Year) Title. American Mineralogist, in press.
DOI: https://doi.org/10.2138/am-2020-7162

= 0.5-1.0). As the reaction proceeds, three moles of *gt* are produced for every mole of *sp* consumed (see reaction [5]). Thus, if the reaction reaches completion (i.e., *sp* is exhausted) the same number of moles of Fe^{3+} that were initially in the *sp* are dissolved in the larger number of moles of *gt*, leading to a lower concentration of Fe^{3+} in the *gt*, and all other things being equal, this would correspond to a lower fO_2. If, as Ballhaus and Frost (1994) assumed, the reaction never goes to completion (i.e., there is always residual Cr^{3+}-rich *sp*), the extent of the decrease in fO_2 due to this reaction would depend on the value of $D(Fe^{3+})_{gt/sp}$, such that at a given extent of reaction more of the Fe^{3+} would be retained in the *sp* at lower D values and the predicted decrease in fO_2 due to this reaction would be smaller than if the D were larger (see Fig. 3 in Ballhaus and Frost, 1994): at 90% reaction, fO_2 is predicted to decrease by ~0.3-0.4 log units for $D(Fe^{3+})_{gt/sp} = 0.5$ and by ~1.5 log units for $D(Fe^{3+})_{gt/sp} = 1.0$. Note that in contrast to the effects of decreasing Fe^{3+}+ in *sp* due to its increasing modal in abundance on conversion of *plag* lherzolite to *sp* lherzolite, which was the basis of their prediction of a large decrease in fO_2 due to such a transformation, in the case of the *sp* -to- *gt*-lherzolite transformation, Ballhaus and Frost (1994) attributed the fO_2 shift to a transfer of Fe^{3+} from one phase (*sp*) to another (*gt*) as the reaction proceeds.

The prediction of Ballhaus and Frost (1994) and Ballhaus (1995) that the fO_2 *decreases* by ~0.4-1.5 orders of magnitude when *sp* lherzolite converts to *gt* lherzolite is opposite in sign to our results, which predict an *increase* in fO_2 of the DMM peridotite composition we have modeled of ~0.5 orders of magnitude over the narrow *P* interval of the *sp*→*gt*-lherzolite transition followed by an additional ~0.5 order of magnitude increase within the *gt*-lherzolite facies up to ~30 kbar for the JH-15 model relative to a metastable *gt*-+*sp*-free assemblage (Fig. 2b); Jennings and Holland (2015) obtained similar result for ΔFMQ also using the JH-15 model for a fertile peridotite (see their Fig. 13). Modeling using pMELTS predicts a continuous increase of ~1 order of magnitude relative to a metastable *gt*-free assemblage from the *gt*-in boundary at ~20 kbar up to 40 kbar (Fig. 2a).

This is a preprint, the final version is subject to change, of the American Mineralogist (MSA)
Cite as Authors (Year) Title. American Mineralogist, in press.
DOI: https://doi.org/10.2138/am-2020-7162

The difference between our results and those of Ballhaus and Frost (1994) and Ballhaus (1995) reflects two factors:

- Ballhaus and Frost (1994) assumed that the effects of *px* could be neglected because their modal abundances of *opx* and *cpx* do not change significantly at this (or the *plag*→*sp*-lherzolite) phase transition. However, according to both of the models applied here, the *px* abundances decrease considerably as the *gt*-in boundary is crossed going up *P*, and as a consequence Fe^{3+} is passively enriched in the *px*, resulting in the modeled increases in fO_2. It is also important that both models we have used yield the result that most of the Fe^{3+} in the system is in the *px* at *gt*-in (>50% for pMELTS and >90% for JH-15; see Figs. 4a and 4b); and at *sp*-out, where *sp* has been exhausted and the amount of garnet has reached ~10 wt. %, the JH-15 model still has >90% of the Fe^{3+} in the *px*. Thus, although by 40 kbar in the JH-15 model, ~50% of the Fe^{3+} in the system has transferred from *px* into *gt*, the assumption by Ballhaus and Frost (1994) and Ballhaus (1995) that *px* is not a major reservoir for Fe^{3+} is the primary source of the difference between our results and theirs. Although ongoing improvements to the pMELTS and JH-15 thermodynamic models can be expected to lead to changes in the details, unless these models are significantly miscalibrated in their treatment of Fe^{3+} in *px*, the predicted increase in fO_2 near the low-*P* end of the *gt*-lherzolite facies is probably robust.
- Based on the JH-15 model, $D(Fe^{3+})_{gt/sp}$ is ~0.13-0.15 in the narrow interval over which *gt* and *sp* coexist at 1100°C. This is significantly lower than the values of 0.5-1.0 assumed by Ballhaus and Frost (1994) and Ballhaus (1995) and would diminish significantly and perhaps reverse their calculated decrease in fO_2 on incomplete reaction of *sp* lherzolite to *gt* lherzolite. We note, however, that as described above, stronger partitioning of Fe^{3+} into *gt* relative to *px* with increasing *P* is predicted by the JH-15 model (Fig. 3b2) to result eventually in a decrease in fO_2 relative to the maximum at *P* ~30 kbar (Fig. 2b) for reasons related to those given by Ballhaus and Frost (1994) and Ballhaus (1995) for their expectation of a decrease in fO_2 in the *gt*-lherzolite field relative to a *sp*-bearing, *gt*-free assemblage. It is conceivable that at high

This is a preprint, the final version is subject to change, of the American Mineralogist (MSA)
Cite as Authors (Year) Title. American Mineralogist, in press.
DOI: https://doi.org/10.2138/am-2020-7162

enough *P* (beyond the 40 kbar upper *P* limit of our calculations) enough of the Fe^{3+} will have transferred to *gt* from *px* such that a situation similar to the end-state of their calculation will have been achieved and the fO_2 will have decreased relative to that a metastable *gt*-free lherzolite, as they predict. However, based on our analysis, this is not relevant to the lower *P* range of the *gt*-lherzolite facies modeled here, where the *gt* is predicted to be relatively Fe^{3+}-poor and reactions involving consumption of *px* (reactions [5] and [6]) lead to increases in the activity of Fe^{3+}-bearing components and thereby result in a significant increase in fO_2 relative to a metastable *gt*-absent assemblage (Fig. 2d).

Although we did not apply the pMELTS and JH-15 models to *P* >40 kbar, it is nevertheless possible to connect our results to those obtained by others for the deeper upper mantle and transition zone. As mentioned above, Jennings and Holland (2015) applied the JH-15 model to the KLB-1 fertile peridotite on isotherms at 800, 1100, and 1400°C and along the solidus from 1 bar to 60 kbar, and Miller et al. (2016) applied it to the composition of a moderately depleted peridotite from the Siberian craton (Y-17) on a model geotherm from 30 to 70 kbar. ΔFMQ from their calculations under subsolidus conditions decreases continuously with increasing *P* above ~30 kbar, plausibly reflecting both the effects on fO_2 of continued transfer of Fe^{3+} from *px* to *gt* discussed previously and the large, negative standard-state volume change for the skiagite-forming reaction (2 fayalite + ferrosilite + ½ O_2 = skiagite) relative to that of the FMQ buffer, which leads, even for a phase assemblage with essentially unchanging phase abundances and compositions, to a large decrease in ΔFMQ (e.g., Gudmundsson and Wood, 1995; Frost and McCammon, 2008; Miller et al., 2016). Despite the differences in the modeled peridotite compositions, the calculated trends of ΔFMQ vs. *P* from Jennings and Holland (2015) are nearly identical to ours where they overlap (1100°C, <40 kbar); likewise, the slope in ΔFMQ vs. *P* from Miller et al. (2016) at 30-40 kbar is similar to ours, although somewhat steeper, perhaps reflecting at least in part the difference between an isothermal path and the geotherm they modeled.

This is a preprint, the final version is subject to change, of the American Mineralogist (MSA)
Cite as Authors (Year) Title. American Mineralogist, in press.
DOI: https://doi.org/10.2138/am-2020-7162

As *P* increases beyond the point at which most of Fe^{3+} in the peridotite has transferred from *px* to *gt*, we anticipate that, relative to a metastable *ol*+*px* assemblage, the fO_2 will not initially change significantly, because of the probable absence of major changes in phase abundances or redistribution of Fe^{3+}, although ΔFMQ will continue to decrease (e.g., Wood et al., 1990; Gudmundsson and Wood, 1995; Frost and McCammon, 2008; Jennings and Holland, 2015; Miller et al., 2016). However, Fe^{3+}-poor *px* progressively transforms into majorite components in the *gt* with further increases in *P*, and this is expected to lead to dilution of Fe^{3+} in the *gt*, and thus to decreasing fO_2 relative to metastable assemblages in which this *px* →*gt* transformation has not occurred (O'Neill et al., 1993; Ballhaus, 1995; Rohrbach et al., 2007; Frost and McCammon, 2008), analogous to what we and Ballhaus and Frost (1994) and Ballhaus (1995) propose to account for the large decrease in fO_2 with increasing *P* across the *plag*-lherzolite field. With further increases in *P* into the transition zone, the Fe^{3+} in the *gt* is expected to partition in significant amounts into ringwoodite and wadsleyite, further diminishing the Fe^{3+} content of the *gt* and thus leading to an even greater decrease in fO_2 relative to metastable assemblages without these phases (O'Neill et al., 1993; Frost and McCammon, 2008); this predicted change in fO_2 due to redistribution of Fe^{3+} is analogous to the explanation we have for the decrease in fO_2 relative to a *gt*±*sp*-free metastable assemblage at $P \gtrsim 30$ kbar, reflecting the progressive transfer of Fe^{3+} from *px* to *gt*. These anticipated changes in fO_2 at *P*s beyond those we have considered are expected to be manifested whether fO_2 is expressed relative to an appropriate metastable reference assemblage or as ΔFMQ.

Effects of *T* and bulk composition

We have emphasized the effects of *P* on changes in fO_2 driven by heterogeneous equilibria in peridotites because the effects of *T* are minor in comparison. This is illustrated in Figures 1c-1f, where the trends in fO_2 for a melt-free DMM peridotite relative to FMQ or relative to a metastable *ol*+*opx*+*cpx*±*sp* assemblage are shown to be essentially unchanged with increasing *T* other than a widening of the *sp*-lherzolite facies (mostly due a positive *P*-*T* slope of the *gt*-in

This is a preprint, the final version is subject to change, of the American Mineralogist (MSA)
Cite as Authors (Year) Title. American Mineralogist, in press.
DOI: https://doi.org/10.2138/am-2020-7162

curve) and overall decreases in ΔFMQ and in fO_2 normalized to a metastable *ol*+*opx*+*cpx*±*sp* assemblage at constant *P* with increasing *T*. This latter effect is only present outside the *sp*-lherzolite facies for fO_2 values normalized to the metastable assemblages because they are constant at zero for the pMELTS model and nearly so for the JH-15 model. Jennings and Holland (2015) show similarly small trends for ΔFMQ for KLB-1 as functions of *T*. Given the minor effects of *T* compared to those of *P*, trends along isentropes would be similar to the isothermal trends shown in Figures 2 and 3 and by Jennings and Holland (2015).

Although our discussion has focused on the DMM composition, our conclusion that heterogeneous equilibria among Al-rich phases in peridotites are the principal drivers of changes in fO_2 with increasing *P* predicts that the fO_2 changes (whether in absolute fO_2, ΔFMQ, or relative to metastable *ol*+*opx*+*cpx*±*sp* assemblages) displayed by our modeling across the *plag*- and *gt*-lherzolite facies will diminish with progressive depletion due to melt extraction, reflecting the decrease in the Al contents of peridotites as a function of depletion. In order to determine the predicted magnitude of the effects of depletion, we ran pMELTS calculations on a Cr^{3+}-free equivalent of the moderately depleted Y-17 *gt* lherzolite (~1.4 wt. % Al_2O_3, compared to ~4.0 wt. % in DMM) modeled by Miller et al. (2016), assuming an Fe_2O_3 content of 0.25 wt. %, similar to that used in our modeling of DMM. Normalized to a metastable *ol*+*opx*+*cpx*+*sp* assemblage, fO_2 for Y-17 decreases by ~1.6 log units from 1 bar to *plag*-out (vs. a ~2.2 log units decrease for the Cr^{3+}-free DMM composition) and increases by ~1.1 log units from *gt*-in to 40 kbar (vs. a ~2.2 log unit increase for the Cr^{3+}-free DMM composition). Although more extensive and systematic modeling to explore the effects of progressive depletion on the phase-equilibrium-driven changes in the fO_2 of peridotite should be conducted – including the decrease in Fe^{3+} content of the peridotite with progressive melt extraction (Pearson et al., 2003; Cottrell and Kelley, 2011; Sorbadere et al., 2018) – this preliminary set of results for a less fertile, Al-poor peridotite is consistent with our conclusion that the *P*-dependent changes in fO_2 for the DMM peridotite composition are driven by reactions involving the major Al-bearing phases.

This is a preprint, the final version is subject to change, of the American Mineralogist (MSA)
Cite as Authors (Year) Title. American Mineralogist, in press.
DOI: https://doi.org/10.2138/am-2020-7162

Implications

(1) Both the pMELTS and JH-15 models predict significant variations in fO_2 for a peridotite of constant bulk composition (including its oxygen content) under stable and metastable subsolidus conditions with increasing *P*. For example, based on the JH-15 model, at 1100°C, the fO_2 relative to a metastable *ol*+*opx*+*cpx* assemblage decreases by ~1.25 log units as the normative abundance of *plag* decreases from its 1 bar value to zero at the upper *P* limit of the *plag*-lherzolite facies. The modeled fO_2 varies little across the *sp*-lherzolite facies and then increases by ~1 log unit up to a maximum at ~30 kbar with the progressive formation of *gt*, above which it decreases by ~0.1 log units. Similar variations are also predicted by the pMELTS model. These relatively large predicted variations in fO_2 do not primarily reflect heterogeneous equilibria that redistribute Fe^{3+} between phases. Instead, according to both models, most of the Fe^{3+} in the peridotite remains in *px* across this *P* range, and the changes in fO_2 are primarily driven by changes in the non-Fe^{3+}-bearing components of the *px* associated with reactions that generate or consume the major aluminous phases (e.g., *plag*, *sp*, *gt*). Reactions that *generate* non-Fe^{3+}-bearing *px* components with increasing *P* (e.g., reactions [1], [2], and [3] in the *plag*-lherzolite facies) lead to dilution of Fe^{3+} in *px* and decreases in its activity and thus to a decrease in fO_2. Reactions that *consume* non-Fe^{3+}-bearing *px* components with increasing *P* (e.g., reactions [5] and [6] in the *gt*-lherzolite facies) lead to enrichment of Fe^{3+} in residual *px* and increases in its activity, and thus to an increase in fO_2. Such reactions – which are responsible for the well-known sequence of *plag*→*sp*→*gt* lherzolite with increasing *P* and the topology in *P*-*T* space of alumina isopleths in *px* – do not directly produce, consume, or transfer significant Fe^{3+}-bearing components, yet they indirectly (or passively) drive the systematic changes in fO_2 with *P*. Most importantly, these fO_2 changes are predicted to be simply and strongly correlated with the well-known dominant changes in phase equilibria and mineral chemistry of peridotites in the upper ~100 km of the upper mantle, and they are of comparable magnitude to the variations in fO_2 observed within suites of natural basalts and peridotites. The small decrease in

This is a preprint, the final version is subject to change, of the American Mineralogist (MSA)
Cite as Authors (Year) Title. American Mineralogist, in press.
DOI: https://doi.org/10.2138/am-2020-7162

modeled fO_2 relative to a metastable *ol*+*opx*+*cpx* assemblage using JH-15 from 30 kbar to 40 kbar probably reflects the competition between the effects of *px* consumption to produce *gt* and the progressive transfer of Fe^{3+} from *px* to *gt* with increasing *P*.

(2) In analyzing the changes in fO_2 predicted by the pMELTS and JH-15 models, we relied heavily on the ability of these thermodynamic models to probe metastable states: First we were able to demonstrate the importance of specific phases in producing the observed changes by selectively excluding them from the equilibrium assemblages; for example, if an effect on fO_2 appeared when a particular phase was allowed to appear in the stable or metastable assemblage but disappeared when the phase was excluded from the assemblage, we inferred that this phase played a role in producing the observed effect. Second, rather than normalizing the modeled fO_2 to standard buffers such as FMQ, we emphasized normalizations to metastable assemblages (e.g., *ol*+*opx*+*cpx*) that lacked the dominant aluminous phases. This allowed isolation of the quantitative effects of the reactions that produce variations in fO_2 by comparing the fO_2 of the same composition at the same *P* and *T* of assemblages with and without these Al-rich phases.

(3) It is widely accepted that the ΔFMQ values of peridotites decrease continuously with increasing *P* in the mantle, but our results on the DMM peridotite composition and those of Jennings and Holland (2015) on the fertile KLB-1 peridotite composition demonstrate a more complex trend in the upper ~100 km of the upper mantle: At constant *T*, ΔFMQ decreases with increasing *P* across the *plag*-lherzolite field; followed by roughly constant ΔFMQ across the *sp*-lherzolite field; this is followed first by a steep increase from just above *gt*-in up to *sp*-out (or to where the residual *sp* is Cr^{3+}-rich) and then by a slower, concave down increase in ΔFMQ across the *gt*-lherzolite field to a maximum at ~20-30 kbar (at 1100°C), above which ΔFMQ decreases. From this point on, the widely accepted trend of decreasing ΔFMQ probably prevails (although for *P* up to 70 kbar, the decrease is smaller than has been generally supposed; Miller et al., 2016), reflecting first the continuing effects of transfer of Fe^{3+} from *px* to *gt*, then dilution of Fe^{3+} in the *gt* due to transfer of the dominant silicate

This is a preprint, the final version is subject to change, of the American Mineralogist (MSA)
Cite as Authors (Year) Title. American Mineralogist, in press.
DOI: https://doi.org/10.2138/am-2020-7162

components of the *px* into *gt* as majoritic components, and finally to transfer of Fe^{3+} from majoritic *gt* to ringwoodite and wadsleyite (Frost and McCammon, 2008).

(4) The overall trend in absolute fO_2 (and thus in μO_2) with increasing *P* up to 40 kbar based on our results is to higher values (Figs. 3a1 and 3b1). The only deviation from this is in the *plag*-lherzolite field, where the decrease in absolute fO_2 due to reaction of *ol* + *plag* to form *px* components is large enough to reverse the overall trend toward increasing absolute fO_2 with increasing *P*. The results of Jennings and Holland (2015) extend this trend to increasing absolute fO_2 with increasing *P* to 60 kbar (based on converting the ΔFMQ values in their Figure 13 to absolute fO_2). The trend in absolute fO_2 with *P* is concave downward outside the *plag*-lherzolite field, and it is possible that absolute fO_2 decreases beyond some higher *P* outside of the range of current calculations. The well-known trend to more negative values of ΔFMQ with increasing *P* above ~30 kbar occurs because even though the calculated absolute fO_2 of the DMM peridotite and that of the FMQ buffer both increase with *P*, the absolute fO_2 of the FMQ buffer increases more steeply (see Figs. 3a and 3b).

Thus, based on the models presented here, μO_2 is to predicted to increase with *P* along an isotherm from ~10 kbar to at least 60 kbar in an isocompositional mantle corresponding to DMM. This increase in μO_2 means that oxygen would flow from peridotite at higher *P* to peridotite at the same *T* but lower *P* in contact across a rigid barrier that is capable of maintaining the difference in P but is semi-permeable with respect to oxygen; this would continue until μO_2 is equalized in the high and low *P* peridotites. This flow of oxygen due to the higher absolute fO_2 of the higher *P* peridotite would occur despite the fact that the higher *P* peridotite has a lower ΔFMQ, which might be misinterpreted as suggesting that it is more reduced in an absolute sense and that oxygen would flow in the opposite direction. Although the conditions of this thought experiment are unlikely to be approximated in nature, the point is that it is important to take care in drawing conclusions from use of reference frames that depend on the thermodynamic properties of buffer assemblages.

This is a preprint, the final version is subject to change, of the American Mineralogist (MSA)
Cite as Authors (Year) Title. American Mineralogist, in press.
DOI: https://doi.org/10.2138/am-2020-7162

(5) The interpretation of the fO_2 variations we have modeled as being driven by phase changes among the dominant Al-rich phases in the upper ~100 km of the mantle suggests that these variations will be progressively muted in peridotites increasingly depleted by extraction of melt because the Al contents of peridotites decrease significantly with progressive depletion. We have validated this suggestion with limited calculations using pMELTS, but more extensive applications of these models are necessary to document and understand fully the effects on the trends we have discussed with major element composition. Note that the effects of T are minor compared to those of P, and as a consequence the results would be similar along isotherms and isentropes.

(6) Returning to the issues raised in the Introduction, numerous studies have documented several orders of magnitude variation in ΔFMQ of terrestrial basaltic magmas and mantle peridotites. The range of fO_2 among unaltered peridotites provides direct evidence of variability in the mantle, and although processes such as crystallization, assimilation, and degassing can affect the fO_2 of a magma, it is probable that at least some – perhaps most – of the range of fO_2 observed in relatively primitive magmas reflects variations inherited from their mantle sources. These variations in the fO_2 of basalts and their mantle sources have mostly been attributed to variations in the chemical compositions of their sources (including their oxygen contents) due, for example, to subduction of oxidizing agents such as fluids, sediments, and altered oceanic crust or to the opposing effects of subducted organic material; to control by equilibration with fluids (especially graphite- or diamond-saturated fluids); or to the effects of partial melting (e.g., depletion of Fe^{3+} in the residue and the resulting reduction). However, our thermodynamic modeling and its interpretation suggest that the effects of P- and T-dependent phase equilibria on ΔFMQ of a relatively fertile subsolidus peridotite of constant composition can be >1 order of magnitude between 1 bar and 40 kbar, which is comparable to most of the variability among peridotites and within suites of each of the most abundant basaltic magma types on Earth. The results of recent experiments (Davis and Cottrell, 2018; Sorbadere et al., 2018) suggest that the fO_2 values of partial melts may

remain similar to those of their unmelted peridotite sources up to a few tens of percent partial melting. This suggests in turn that the effects of heterogeneous phase equilibria on the fO_2 values of subsolidus DMM peridotite presented here may be manifested in the fO_2 values of melts produced by low degrees of partial melting of relatively fertile peridotites.

Overall, the systematic and significant effects of phase equilibria in subsolidus peridotite on fO_2 that we have modeled here are expected to be superimposed in the mantle on the more commonly invoked sources of fO_2 variability in magmas and peridotites that result in variations in bulk composition (especially Fe^{3+}/Fe^{2+} of the mantle). Consequently, such effects should also be considered in efforts to understand observed variations in the oxygen fugacities of magmas and their mantle sources of up to ~1-2 orders of magnitude.

Acknowledgments

We thank M.B. Baker, J.D. Blundy, E. Cottrell, J.M. Eiler, and B.J. Wood for helpful discussions and suggestions, and E. Cottrell, F. Davis, and B. Scaillet for helpful reviews. OS was supported at Caltech by a geology option postdoctoral fellowship and by a fellowship from Trinity College, Cambridge. PDA and PMA acknowledge support from NSF via award EAR-1550934. This manuscript was based on the first author's 2017 Roebling Medal lecture.

References

Antoshechkina, P.M., and Ghiorso, M.S. (2018) MELTS for MATLAB: A new educational and research tool for computational thermodynamics. Eos, Transactions, American Geophysical Union.

Arculus, R.J. (1985) Oxidation status of the mantle: past and present. Annual Review of Earth and Planetary Sciences, 13(1), 75-95.

Asimow, P.D., and Ghiorso, M.S. (1998) Algorithmic modifications extending MELTS to calculate subsolidus phase relations. American Mineralogist, 83(9-10), 1127-1132.

Aulbach, S., and Stagno, V. (2016) Evidence for a reducing Archean ambient mantle and its effects on the carbon cycle. Geology, 44(9), 751-754.

Ballhaus, C. (1995) Is the upper mantle metal-saturated? Earth and Planetary Science Letters, 132(1-4), 75-86.

Ballhaus, C., Berry, R.F., and Green, D.H. (1990) Oxygen fugacity controls in the Earth's upper mantle. Nature, 348(6300), 437-440.

Ballhaus, C., and Frost, B.R. (1994) The generation of oxidized CO_2-bearing basaltic melts from reduced CH_4-bearing upper mantle sources. Geochimica et Cosmochimica Acta, 58(22), 4931-4940.

Bénard, A., Klimm, K., Woodland, A.B., Arculus, R.J., Wilke, M., Botcharnikov, R.E., Shimizu, N., Nebel, O., Rivard, C., and Ionov, D.A. (2018a) Oxidising agents in sub-arc mantle melts link slab devolatilisation and arc magmas. Nature Communications, 9(1), 3500.

Bénard, A., Woodland, A.B., Arculus, R.J., Nebel, O., and McAlpine, S.R. (2018b) Variation in sub-arc mantle oxygen fugacity during partial melting recorded in refractory peridotite xenoliths from the West Bismarck Arc. Chemical Geology, 486, 16-30.

Berman, R.G. (1988) Internally-consistent thermodynamic data for minerals in the system Na_2O-K_2O-CaO-MgO-FeO-Fe_2O_3-Al_2O_3-SiO_2-TiO_2-H_2O-CO_2. Journal of Petrology, 29(2), 445-522.

Berndt, J., Koepke, J., and Holtz, F. (2004) An experimental investigation of the influence of water and oxygen fugacity on differentiation of MORB at 200 MPa. Journal of Petrology, 46(1), 135-167.

Birner, S.K., Cottrell, E., Warren, J.M., Kelley, K.A., and Davis, F.A. (2018) Peridotites and basalts reveal broad congruence between two independent records of mantle f_{O2} despite local redox heterogeneity. Earth and Planetary Science Letters, 494, 172-189.

Blundy, J.D., Brodholt, J.P., and Wood, B.J. (1991) Carbon–fluid equilibria and the oxidation state of the upper mantle. Nature, 349(6307), 321.

Borghini, G., Fumagalli, P., and Rampone, E. (2009) The stability of plagioclase in the upper mantle: subsolidus experiments on fertile and depleted lherzolite. Journal of Petrology, 51(1-2), 229-254.

Brounce, M., Kelley, K.A., Cottrell, E., and Reagan, M.K. (2015) Temporal evolution of mantle wedge oxygen fugacity during subduction initiation. Geology, 43(9), 775-778.

Brounce, M., Stolper, E.M., and Eiler, J. (2017) Redox variations in Mauna Kea lavas, the oxygen fugacity of the Hawaiian plume, and the role of volcanic gases in Earth's oxygenation. Proceedings of the National Academy of Sciences, 114(34), 8997-9002.

Brounce, M.N., Kelley, K.A., and Cottrell, E. (2014) Variations in $Fe^{3+}/\Sigma Fe$ of Mariana arc basalts and mantle wedge fO_2. Journal of Petrology, 55(12), 2513-2536.

Bryndzia, L.T., and Wood, B.J. (1990) Oxygen thermobarometry of abyssal spinel peridotites: the redox state and C–O–H volatile composition of the Earth's sub-oceanic upper mantle. American Journal of Science, 290(10), 1093-1116.

Buddington, A.F., and Lindsley, D.H. (1964) Iron-titanium oxide minerals and synthetic equivalents. Journal of Petrology, 5(2), 310-357.

Burgisser, A., and Scaillet, B. (2007) Redox evolution of a degassing magma rising to the surface. Nature, 445(7124), 194-197.

Carmichael, I.S.E. (1991) The redox states of basic and silicic magmas: a reflection of their source regions? Contributions to Mineralogy and Petrology, 106, 129-141.

Christie, D.M., Carmichael, I.S.E., and Langmuir, C.H. (1986) Oxidation states of mid-ocean ridge basalt glasses. Earth and Planetary Science Letters, 79(3-4), 397-411.

Connolly, J.A.D. (2009) The geodynamic equation of state: what and how. Geochemistry, Geophysics, Geosystems, 10(10).

Cottrell, E., and Kelley, K.A. (2011) The oxidation state of Fe in MORB glasses and the oxygen fugacity of the upper mantle. Earth and Planetary Science Letters, 305(3), 270-282.

Cottrell, E., and Kelley, K.A. (2013) Redox heterogeneity in mid-ocean ridge basalts as a function of mantle source. Science, 1233299.

Davis, F.A., and Cottrell, E. (2018) Experimental investigation of basalt and peridotite oxybarometers: Implications for spinel thermodynamic models and Fe^{3+} compatibility during generation of upper mantle melts. American Mineralogist, 103(7), 1056-1067.

Delano, J.W. (2001) Redox history of the Earth's interior since ~3900 Ma: implications for prebiotic molecules. Origins of Life and Evolution of the Biosphere, 31(4-5), 311-341.

Denbigh, K. (1971) The Principles of Chemical Equilbrium (Third Edition). 516 p. Cambridge University Press.

Eggler, D.H. (1983) Upper mantle oxidation state: Evidence from olivine-orthopyroxene-ilmenite assemblages. Geophysical Research Letters, 10(5), 365-368.

Frost, B.R. (1991) Introduction to oxygen fugacity and its petrologic importance. Reviews in Mineralogy and Geochemistry, 25(1), 1-9.

Frost, B.R., and Lindsley, D.H. (1991) Occurrence of iron-titanium oxides in igneous rocks. Reviews in Mineralogy and Geochemistry, 25(1), 433-468.

Frost, D.J., Liebske, C., Langenhorst, F., McCammon, C.A., Trønnes, R.G., and Rubie, D.C. (2004) Experimental evidence for the existence of iron-rich metal in the Earth's lower mantle. Nature, 428(6981), 409.

Frost, D.J., and McCammon, C.A. (2008) The redox state of Earth's mantle. Annual Review of Earth and Planetary Sciences, 36, 389-420.

Gaetani, G.A. (2016) The behavior of $Fe^{3+}/\Sigma Fe$ during partial melting of spinel lherzolite. Geochimica et Cosmochimica Acta, 185, 64-77.

Gaillard, F., Scaillet, B., and Arndt, N.T. (2011) Atmospheric oxygenation caused by a change in volcanic degassing pressure. Nature, 478(7368), 229-232.

Gaillard, F., Scaillet, B., Pichavant, M., and Iacono-Marziano, G. (2015) The redox geodynamics linking basalts and their mantle sources through space and time. Chemical Geology, 418, 217-233.

Gasparik, T. (2014) Phase diagrams for geoscientists (Second Edition). 462 p. Springer.

Ghiorso, M.S., Hirschmann, M.M., Reiners, P.W., and Kress III, V.C. (2002) The pMELTS: A revision of MELTS for improved calculation of phase relations and major element partitioning related to partial melting of the mantle to 3 GPa. Geochemistry, Geophysics, Geosystems, 3(5), 1-35.

Green, D.H., and Hibberson, W. (1970) The instability of plagioclase in peridotite at high pressure. Lithos, 3(3), 209-221.

Green, D.H., and Ringwood, A.E. (1970) Mineralogy of peridotitic compositions under upper mantle conditions. Physics of the Earth and Planetary Interiors, 3, 359-371.

Grocke, S.B., Cottrell, E., de Silva, S., and Kelley, K.A. (2016) The role of crustal and eruptive processes versus source variations in controlling the oxidation state of iron in Central Andean magmas. Earth and Planetary Science Letters, 440, 92-104.

Gudmundsson, G., and Wood, B.J. (1995) Experimental tests of garnet peridotite oxygen barometry. Contributions to Mineralogy and Petrology, 119(1), 56-67.

Haggerty, S.E. (1976) Opaque igneous oxides in terrestrial igneous rocks. In A. El Goresy, S.E. Haggerty, S.E. Huebner, D.H. Lindsley, and D. Rumble, III, Eds. Oxide Minerals, 3, p. HG101-HG300. Mineralogical Society of America.

Hamilton, D.L., and Anderson, G.M. (1967) Effects of water and oxygen pressures on the crystallization of basaltic magmas. In H.H. Hess, and A. Poldervaart, Eds. Basalts: The Poldervaart Treatise on Rocks of Basaltic Composition, 1, p. 445-482. Interscience Publishers, London Sydney.

Hartley, M.E., Shorttle, O., Maclennan, J., Moussallam, Y., and Edmonds, M. (2017) Olivine-hosted melt inclusions as an archive of redox heterogeneity in magmatic systems. Earth and Planetary Science Letters, 479, 192-205.

Hirschmann, M.M. (2012) Magma ocean influence on early atmosphere mass and composition. Earth and Planetary Science Letters, 341, 48-57.

Jennings, E.S., and Holland, T.J.B. (2015) A simple thermodynamic model for melting of peridotite in the system NCFMASOCr. Journal of Petrology, 56(5), 869-892.

Kasting, J.F., Eggler, D.H., and Raeburn, S.P. (1993) Mantle redox evolution and the oxidation state of the Archean atmosphere. Journal of Geology, 101(2), 245-257.

Kelley, K.A., and Cottrell, E. (2009) Water and the oxidation state of subduction zone magmas. Science, 325(5940), 605-607.

Kelley, K.A., and Cottrell, E. (2012) The influence of magmatic differentiation on the oxidation state of Fe in a basaltic arc magma. Earth and Planetary Science Letters, 329, 109-121.

Kress, V.C., and Carmichael, I.S.E. (1991) The compressibility of silicate liquids containing Fe_2O_3 and the effect of composition, temperature, oxygen fugacity and pressure on their redox states. Contributions to Mineralogy and Petrology, 108(1-2), 82-92.

Kump, L.R., and Barley, M.E. (2007) Increased subaerial volcanism and the rise of atmospheric oxygen 2.5 billion years ago. Nature, 448(7157), 1033.

Lee, C.-T.A., Lee, T.C., and Wu, C.-T. (2014) Modeling the compositional evolution of recharging, evacuating, and fractionating (REFC) magma chambers: Implications for differentiation of arc magmas. Geochimica et Cosmochimica Acta, 143, 8-22.

Lee, C.-T.A., Leeman, W.P., Canil, D., and Li, Z.-X.A. (2005) Similar V/Sc systematics in MORB and arc basalts: implications for the oxygen fugacities of their mantle source regions. Journal of Petrology, 46(11), 2313-2336.

Lee, C.-T.A., Luffi, P., Le Roux, V., Dasgupta, R., Albarède, F., and Leeman, W.P. (2010) The redox state of arc mantle using Zn/Fe systematics. Nature, 468(7324), 681.

Li, Z.-X.A., and Lee, C.-T.A. (2004) The constancy of upper mantle fO_2 through time inferred from V/Sc ratios in basalts. Earth and Planetary Science Letters, 228(3-4), 483-493.

Lindsley, D., Davis, B., and MacGregor, I. (1964) Ferrosilite ($FeSiO_3$): Synthesis at high pressures and temperatures. Science, 144(3614), 73-74.

MacGregor, I.D. (1967) Mineralogy of model mantle compositions. In P.J. Wyllie, Ed. Ultramafic and Related Rocks, p. 382-393. John Wiley & Sons, Inc., New York.

Macgregor, I.D. (1970) The effect of CaO, Cr_2O_3, Fe_2O_3 and Al_2O_3 on the stability of spinel and garnet peridotites. Physics of the Earth and Planetary Interiors, 3, 372-377.

MacGregor, I.D. (2015) Empirical geothermometers and geothermobarometers for spinel peridotite phase assemblages. International Geology Review, 57(15), 1940-1974.

Mathez, E.A. (1984) Influence of degassing on oxidation states of basaltic magmas. Nature, 310, 371-375.

Mattioli, G.S., Baker, M.B., Rutter, M.J., and Stolper, E.M. (1989) Upper mantle oxygen fugacity and its relationship to metasomatism. The Journal of Geology, 97(5), 521-536.

Miller, W.G., Holland, T.J., and Gibson, S.A. (2016) Garnet and spinel oxybarometers: new internally consistent multi-equilibria models with applications to the oxidation state of the lithospheric mantle. Journal of Petrology, 57(6), 1199-1222.

Moussallam, Y., Edmonds, M., Scaillet, B., Peters, N., Gennaro, E., Sides, I., and Oppenheimer, C. (2016) The impact of degassing on the oxidation state of basaltic magmas: a case study of Kīlauea volcano. Earth and Planetary Science Letters, 450, 317-325.

Moussallam, Y., Longpré, M.-A., McCammon, C., Gomez-Ulla, A., Rose-Koga, E.F., Scaillet, B., Peters, N., Gennaro, E., Paris, R., and Oppenheimer, C. (2019) Mantle plumes are oxidised. Earth and Planetary Science Letters, 527, 115798.

Moussallam, Y., Oppenheimer, C., Scaillet, B., Gaillard, F., Kyle, P., Peters, N., Hartley, M., Berlo, K., and Donovan, A. (2014) Tracking the changing oxidation state of Erebus magmas, from mantle to surface, driven by magma ascent and degassing. Earth and Planetary Science Letters, 393, 200-209.

Mungall, J.E. (2002) Roasting the mantle: Slab melting and the genesis of major Au and Au-rich Cu deposits. Geology, 30(10), 915-918.

Nickel, K. (1986) Phase equilibria in the system SiO_2–MgO–Al_2O_3–CaO–Cr_2O_3 (SMACCR) and their bearing on spinel/garnet lherzolite relationships. Neues Jahrbuch für Mineralogie Abhandlungen, 155, 259-87.

O'Neill, H.S.C. (1981) The transition between spinel lherzolite and garnet lherzolite, and its use as a geobarometer. Contributions to Mineralogy and Petrology, 77(2), 185-194.

O'Neill, H.S.C., Rubie, D.C., Canil, D., Geiger, C.A., Ross, C.R., II, Seifert, F., and Woodland, A.B. (1993) Ferric iron in the upper mantle and in transition zone assemblages: implications for relative oxygen fugacities in the mantle. In E. Takahashi, and R. Jeanloz, Eds. Evolution of the Earth and Planets, p. 73-88. American Geophysical Union and International Union of Geodesy and Geophysics, Washington, DC; Brussels, Belgium.

Obata, M. (1976) The solubility of Al_2O_3 in orthopyroxenes in spinel and plagioclase peridotites and spinel pyroxenite. American Mineralogist, 61, 804-816.

Osborn, E.F. (1959) Role of oxygen pressure in the crystallization and differentiation of basaltic magma. American Journal of Science, 257, 609-647.

Parkinson, I.J., and Arculus, R.J. (1999) The redox state of subduction zones: insights from arc-peridotites. Chemical Geology, 160(4), 409-423.

Pearson, D.G., Canil, D., and Shirey, S.B. (2003) Mantle samples included in volcanic rocks: xenoliths and diamonds. Treatise on Geochemistry, 2, 171-275.

Robinson, J.A.C., and Wood, B.J. (1998) The depth of the spinel to garnet transition at the peridotite solidus. Earth and Planetary Science Letters, 164(1-2), 277-284.

Rohrbach, A., Ballhaus, C., Golla–Schindler, U., Ulmer, P., Kamenetsky, V.S., and Kuzmin, D.V. (2007) Metal saturation in the upper mantle. Nature, 449(7161), 456.

Sack, R.O., and Ghiorso, M.S. (1994) Thermodynamics of multicomponent pyroxenes: III. Calibration of $Fe^{2+}(Mg)_{-1}$, $TiAl_2(MgSi_2)_{-1}$, $TiFe_2^{3+}(MgSi_2)_{-1}$, $AlFe^{3+}(MgSi)_{-1}$, $NaAl(CaMg)_{-1}$, $Al_2(MgSi)_{-1}$ and $Ca(Mg)_{-1}$ exchange reactions between pyroxenes and silicate melts. Contributions to Mineralogy and Petrology, 118(3), 271-296.

Shorttle, O., Moussallam, Y., Hartley, M.E., Maclennan, J., Edmonds, M., and Murton, B.J. (2015) Fe-XANES analyses of Reykjanes Ridge basalts: Implications for oceanic crust's role in the solid Earth oxygen cycle. Earth and Planetary Science Letters, 427, 272-285.

Sorbadere, F., Laurenz, V., Frost, D.J., Wenz, M., Rosenthal, A., McCammon, C., and Rivard, C. (2018) The behaviour of ferric iron during partial melting of peridotite. Geochimica et Cosmochimica Acta, 239, 235-254.

Stagno, V., and Frost, D.J. (2010) Carbon speciation in the asthenosphere: Experimental measurements of the redox conditions at which carbonate-bearing melts coexist with graphite or diamond in peridotite assemblages. Earth and Planetary Science Letters, 300(1-2), 72-84.

Stagno, V., Ojwang, D.O., McCammon, C.A., and Frost, D.J. (2013) The oxidation state of the mantle and the extraction of carbon from Earth's interior. Nature, 493(7430), 84-88.

Stolper, D.A., and Bucholz, C.E. (2019) Neoproterozoic to early Phanerozoic rise in island arc redox state due to deep ocean oxygenation and increased marine sulfate levels. Proceedings of the National Academy of Sciences, 201821847.

Stolper, D.A., and Keller, C.B. (2018) A record of deep-ocean dissolved O_2 from the oxidation state of iron in submarine basalts. Nature, 553(7688), 323.

Tang, M., Erdman, M., Eldridge, G., and Leem, C.-T.A. (2018) The redox "filter" beneath magmatic orogens and the formation of continental crust. Science Advances, 4(5).

Warren, J.M. (2016) Global variations in abyssal peridotite compositions. Lithos, 248, 193-219.
Waters, L.E., and Lange, R.A. (2016) No effect of H_2O degassing on the oxidation state of magmatic liquids. Earth and Planetary Science Letters, 447, 48-59.
Wood, B.J. (1991) Oxygen barometry of spinel peridotites. Reviews in Mineralogy and Geochemistry, 25(1), 417-432.
Wood, B.J., Bryndzia, L.T., and Johnson, K.E. (1990) Mantle oxidation state and its relationship to tectonic environment and fluid speciation. Science, 248(4953), 337-345.
Woodland, A.B., and Koch, M. (2003) Variation in oxygen fugacity with depth in the upper mantle beneath the Kaapvaal craton, Southern Africa. Earth and Planetary Science Letters, 214(1-2), 295-310.
Woodland, A.B., Kornprobst, J., and Wood, B.J. (1992) Oxygen thermobarometry of orogenic lherzolite massifs. Journal of Petrology, 33(1), 203-230.
Woodland, A.B., and O'Neill, H.S.C. (1993) Synthesis and stability of $Fe_3^{2+}Fe_2^{3+}Si_3O_{12}$ garnet and phase relations with $Fe_3Al_2O_{12}$–$Fe_3^{2+}Fe_2^{3+}Si_3O_{12}$ solutions. American Mineralogist, 78(9-10), 1002-1015.
Woodland, A.B., and O'Neill, H.S.C. (1995) Phase relations between $Ca_3Fe_2^{3+}Si_3O_{12}$–$Fe_3^{2+}Fe_2^{3+}Si_3O_{12}$ garnet and $CaFeSi_2O_6$–$Fe_2Si_2O_6$ pyroxene solid solutions. Contributions to Mineralogy and Petrology, 121(1), 87-98.
Workman, R.K., and Hart, S.R. (2005) Major and trace element composition of the depleted MORB mantle (DMM). Earth and Planetary Science Letters, 231(1), 53-72.

Figure captions

Figure 1**.** *P-T* sections for the slightly depleted DMM mantle composition (Workman and Hart, 2005), for which 3% of the Fe is present as Fe^{3+} and Fe is assumed to be the only heterovalent cation. Contours in each panel reflect $\log_{10}fO_2$ in absolute terms or relative to buffers or other assemblages. Panels (**a**), (**c**), and (**e**) on the left were calculated with the pMELTS model (Ghiorso et al., 2002). Panels (**b**), (**d**), and (**f**) on the right were calculated with the JH-15 model (Jennings and Holland, 2015). The "jitters" in some of the contours reflect imperfect convergence of the energy minimizations. The larger "zigzags" in the pMELTS model (most noticeably those labeled *i* and *ii* in panel [**e**]; these are explained in the text and in detail in the caption to Fig. 4) are due to the stabilization of pigeonite at the expense of *opx* + diopsidic *cpx*, which occurs at slightly higher *P* for a given *T* in the metastable *ol*+*opx*+*cpx*+*sp* assemblage than in the stable DMM assemblage. All calculated values of fO_2 in this and subsequent figures are for melt-free assemblages: Below the dashed black solidus curves, the melt-free assemblages are stable; above the solidus, the melt-free assemblages are metastable relative to partially or fully molten assemblages. The *plag*-out and *gt*-in boundaries are shown in green; the fields between these boundaries are labeled by the dominant Al-rich phase (i.e., *plag* lherzolite, *sp* lherzolite, or *gt* lherzolite). Contours in panels (**a**) and (**b**) show absolute values (i.e., unnormalized) of $\log_{10}fO_2$, where fO_2 is in bars. Contours in panels (**c**) and (**d**) show the difference in $\log_{10}fO_2$

This is a preprint, the final version is subject to change, of the American Mineralogist (MSA)
Cite as Authors (Year) Title. American Mineralogist, in press.
DOI: https://doi.org/10.2138/am-2020-7162

between that of the calculated stable assemblage of that of the FMQ buffer ("ΔFMQ"). Contours in panel (**e**) show the difference in $\log_{10} fO_2$ between that of the calculated stable assemblage and that of the stable (in the *sp*-lherzolite facies) or metastable (in the *plag*- and *gt*-lherzolite facies) *ol*+*opx*+*cpx*+*sp* assemblage for the DMM composition calculated using pMELTS. Because the stable and normalizing assemblages are identical in the *sp*-lherzolite facies, the normalized fO_2 is precisely zero in this field. Contours in panel (**f**) show a similar normalization of $\log_{10} fO_2$ relative to a metastable *ol*+*opx*+*cpx* assemblage for the DMM composition in all facies calculated using the JH-15 model. As discussed in the text, (**e**) and (**f**) isolate the effects of Al-rich phases on the fO_2 of lherzolite by comparing the fO_2 of the same composition at the same P and T of assemblages with and without these Al-rich phases. As also discussed in the text, the most prominent feature of this figure, particular panels (**e**) and (**f**), is the pronounced low-fO_2 "well" associated with the *sp*-lherzolite facies in both models. The gray dotted lines in (**a**)-(**d**) are the 1100°C isotherms for the calculations shown in Fig. 2; the grey dashed lines in (**e**) and (**f**) are the 1300°C isotherms for the calculations shown in Figs. 3 and 4.

Figure 2**.** Calculated subsolidus variations for the DMM bulk composition with P at 1300°C of normalized $\log_{10} fO_2$, mole fractions of Al^{3+} and Fe^{3+} in *opx*, and activities of Al_2O_3 and Fe_2O_3 in *opx*. The panels on the left are based on pMELTS; the panels on the right are based on JH-15. (**a**) Isothermal section showing the difference between $\log_{10} fO_2$ of the most stable melt-free assemblage for the DMM composition (which is metastable at low P relative to a partially molten assemblage) and the $\log_{10} fO_2$ of an *ol*+*opx*+*cpx*+*sp* assemblage corresponding to the DMM composition (which is metastable relative to *plag*- and *gt*-bearing assemblages at $\lesssim$ 9 kbar and $\gtrsim$ 19 kbar, respectively) based on pMELTS. (**b**) Isothermal section showing the difference between $\log_{10} fO_2$ of the most stable melt-free assemblage for the DMM composition (which is metastable at low P relative to a partially molten assemblage) and the $\log_{10} fO_2$ of the DMM composition in a metastable *ol*+*opx*+*cpx* assemblage based on JH-15. (**c**) Further metastable results from pMELTS at 1300°C, normalized to an *ol*+*opx*+*cpx*+*sp* assemblage; along the blue

This is a preprint, the final version is subject to change, of the American Mineralogist (MSA)
Cite as Authors (Year) Title. American Mineralogist, in press.
DOI: https://doi.org/10.2138/am-2020-7162

curve, *plag* and *sp* are the only aluminous phases other than *opx* and *cpx* allowed to form, whereas along the purple curve only *gt* and *sp* are allowed. (**d**) Further metastable results from JH-15 at 1300°C, normalized to an *ol*+*opx*+*cpx* assemblage; along the blue curve, *plag* is the only aluminous phase other than *opx* and *cpx*; along the orange curve, *sp* is the only such phase; and along the purple curve, *gt* is the only such phase. (**e, f**) Activities of Al_2O_3 and Fe_2O_3 in *opx* vs. *P* at 1300°C for the pMELTS and JH-15 results shown in panels (**a**) and (**b**) of this figure. For pMELTS the standard states for Al_2O_3 and Fe_2O_3 are chosen to be internally consistent with the Berman (1988) thermodynamic dataset and the *opx* solid solution model (Sack and Ghiorso, 1994); in JH-15 this approach is not possible, so corundum (*cor*) and hematite (*hem*) are used as standard states. Calculations in pMELTS (not shown) using *cor* and *hem* as the standard states result in activities of Al_2O_3 and Fe_2O_3 that are the same in all assemblage phases, by definition, and more closely resemble the JH-15 results (e.g., activity of Al_2O_3 is increased, and activity of Fe_2O_3 is decreased, relative to the results shown in panel [**e**]). (**g**, **h**) Mole fractions of Al^{3+} and Fe^{3+} on a cation basis (equivalent to mole fractions of Al_2O_3 and Fe_2O_3 for *opx* stoichiometry) vs. *P* at 1300°C for the pMELTS and JH-15 results shown in panels (**a**) and (**b**) of this figure. The labels *i* and *ii* in the pMELTS panels indicate discontinuities associated with the stabilization of pigeonite discussed in the text and in the caption to Fig. 4.

Figure 3. Calculated stable subsolidus variations for the DMM bulk composition vs. *P* at 1100°C. The panels on the left (**a1**-**a3**) are based on pMELTS calculations; the panels on the right (**b1**-**b3**) are based on the JH-15 model. (**a1**, **b1**) Absolute (i.e., unnormalized) $\log_{10} fO_2$ is shown in black and ΔFMQ is shown in red. The absolute $\log_{10} fO_2$ of the FMQ buffer is shown as a dashed black curve for reference. (**a2**, **b2**) Mole fractions of Fe^{3+}, on a cation basis, for the phases in the calculated stable assemblages. (**a3**, **b3**) Fractions (by weight) of the phases in the calculated stable assemblages. Phases in the bottom three rows are *ol* (green), *opx* (black), *cpx* (gray), *plag* (blue), *sp* (orange), and *gt* (purple). Phase boundaries (labeled *plag*-out, *gt*-in, *sp*-

This is a preprint, the final version is subject to change, of the American Mineralogist (MSA)
Cite as Authors (Year) Title. American Mineralogist, in press.
DOI: https://doi.org/10.2138/am-2020-7162

out; these labels are referenced to changes in the stable assemblage with increasing *P*) are shown as colored vertical dashed lines.

Figure 4. Calculated distributions of Fe^{3+} between coexisting phases (excluding *ol* and *plag*, which are assumed to contain no Fe^{3+}) in peridotitic assemblages for the DMM bulk compositions based on pMELTS (panels [**a**] and [**c**]) and JH-15 (panels [**b**] and [**d**] as functions of *P* at 1300°C. The y axes in (**a**) and (**c**) (and for each of the subpanels in [**c**] and [**d**]) show for each phase (distinguished by the color coding) the total quantity of Fe^{3+} contained in that phase divided by the total quantity of Fe^{3+} contained in the DMM bulk composition. Panels (**a)** and (**b)** show the results for the most stable melt-free assemblage for the DMM composition (which is metastable at low *P* relative to a partially molten assemblage; i.e., these panels show the Fe^{3+} distributions associated with Figs. 2a and 2b). Panels (**c**) and (**d**) show the results for the various metastable assemblages described in the text and shown in Figs. 2c and 2d. Note that the bottom panels in (**c**) and (**d**) represent the reference assemblages for fO_2 used in Fig. 2. The nearly discontinuous decreases in the fraction of Fe^{3+} in *cpx* with increasing *P* at low *P* in (**a**) and (**c**) (labeled *i* and *ii*, and associated with corresponding changes in the fractions of Fe^{3+} in *opx* and *sp*) reflect the stabilization of pigeonite relative to *opx* + diopsidic *cpx* (i.e., effectively the passage of a diopsidic *cpx* + pigeonite *cpx* + *opx* three-phase triangle over the DMM bulk composition) in the pMELTS calculations at the lowest *P*s. This feature appears at lower *P* in the presence of *plag* (0.75 kbar; labeled *i* in [**a**] and the top panel of [**c**]) than it does when *plag* is suppressed (3.7 kbar; labeled *ii* in the lower two panels of [**c**]). This change in the nature of the *cpx* has only a small effect on the trend in fO_2 with *P*, although it is visible in Figs. 2a and 2c (where the occurrence of the transition in DMM is labeled *i* and the occurrence of the transition in the reference *ol*+*opx*+*cpx*+*sp* assemblage is labeled *ii*). Note that this feature is not present in Fig. 3 because pigeonite is only stabilized above ~1300°C in DMM; also, this feature is not present in the stable subsolidus DMM assemblage, only in the low *P* region in which we show the metastable subsolidus assemblage by suppressing the stabilization of liquid.

This is a preprint, the final version is subject to change, of the American Mineralogist (MSA)
Cite as Authors (Year) Title. American Mineralogist, in press.
DOI: https://doi.org/10.2138/am-2020-7162

Figure 5. Schematic subsolidus phase equilibria in the five-component system FeO-$Fe_{⅔}O$-CaO-$Al_{⅔}O$-$Si_{½}O$ (i.e., FeO-Fe_2O_3-CaO-Al_2O_3-SiO_2 with components and phase compositions all defined on a single-oxygen basis), projected from *ol* (i.e., fayalite, $Fe_{½}Si_{¼}O$) and *cpx* (i.e., hedenbergite, $Ca_{⅙}Fe_{⅙}Si_{⅓}O$) onto the $Si_{½}O$-$Al_{⅔}O$-$Fe_{⅔}O$ plane. As described in the text, although schematic, this model system provides a graphical framework for understanding the sequence of phases and their compositions with increasing *P* as calculated by the pMELTS and JH-15 models for the DMM peridotite compositions. (**a**) Projected positions of the major end members of *px, gt,* and *sp*. (**b**)-(**n**) Sequence of isothermal sections going up in *P*. A model bulk peridotite composition is shown as a green cross at the same location in all panels. Stable phases are shown in red; the *sp* solid solution between magnetite and hercynite is shown as a red line at the base of each triangle, and the *gt* solid solution between skiagite and almandine is shown as a red line in the panels in which it is stable ([**j**]-(**n**]); the projected *opx* solid solution is shown as a red region extending downward from pure ferrosilite (at the $Si_{½}O$ apex) to Fe^{3+}- and Al-bearing compositions. Tie lines are gray, and three-phase triangles (in projection) are blue with a purple interior. All *opx* + *sp* tie lines are drawn assuming $(Fe^{3+}/Al)_{sp}/(Fe^{3+}/Al)_{opx} = 1$; the JH-15 model predicts lower values, the pMELTS model predicts lower to higher values, and partitioning in natural peridotites is ~0.7 (Canil and O'Neill, 1996); variations in this ratio would affect the orientation of the tie lines but not the sequence of assemblages or overall topologies. Although the trends with increasing *P* are unaffected, the model peridotite position and the compositions of coexisting solid solutions have all been exaggerated to unrealistically high Fe^{3+} contents for better visibility. The relation of these diagrams to the output of the pMELTS and JH-15 models is described in detail in the text.

Figure 6. Enlargement of the upper right regions of the schematic phase diagrams from (**a**) Fig. 5b for the *plag*-lherzolite facies; (**b**) Fig. 5n for the *gt*-lherzolite facies if the *gt* is assumed to be Ca- and Fe^{3+}-free (i.e., pure almandine); and (**c**) Fig. 5n for the *gt*-lherzolite facies if the *gt* is

This is a preprint, the final version is subject to change, of the American Mineralogist (MSA)
Cite as Authors (Year) Title. American Mineralogist, in press.
DOI: https://doi.org/10.2138/am-2020-7162

assumed to have a non-negligible quantity of Fe^{3+}, which increases with increasing *P* on the skiagite-almandine join ("*gt* ss"). These diagrams are described in detail in the text to illustrate graphically the opposite effects on the Fe^{3+} content of *opx* (and hence on fO_2) of the production of quadrilateral and aluminous *px* components as *P* increases across the *plag*-lherzolite facies and the consumption of these *px* components as *P* increases across the *gt*-lherzolite facies. As in Fig. 5, the Fe^{3+} contents of the bulk peridotite (green dot) and of the *opx* coexisting with *plag* in (**a**) and with *gt* in (**b**) have been exaggerated for the purposes of this illustration. The Fe^{3+} contents of the bulk peridotite, *px*, and *gt* have been even further exaggerated in (**c**). The black dotted lines in each panel approximate constant Fe^{3+} contents, with the lines to the left having higher Fe^{3+}.

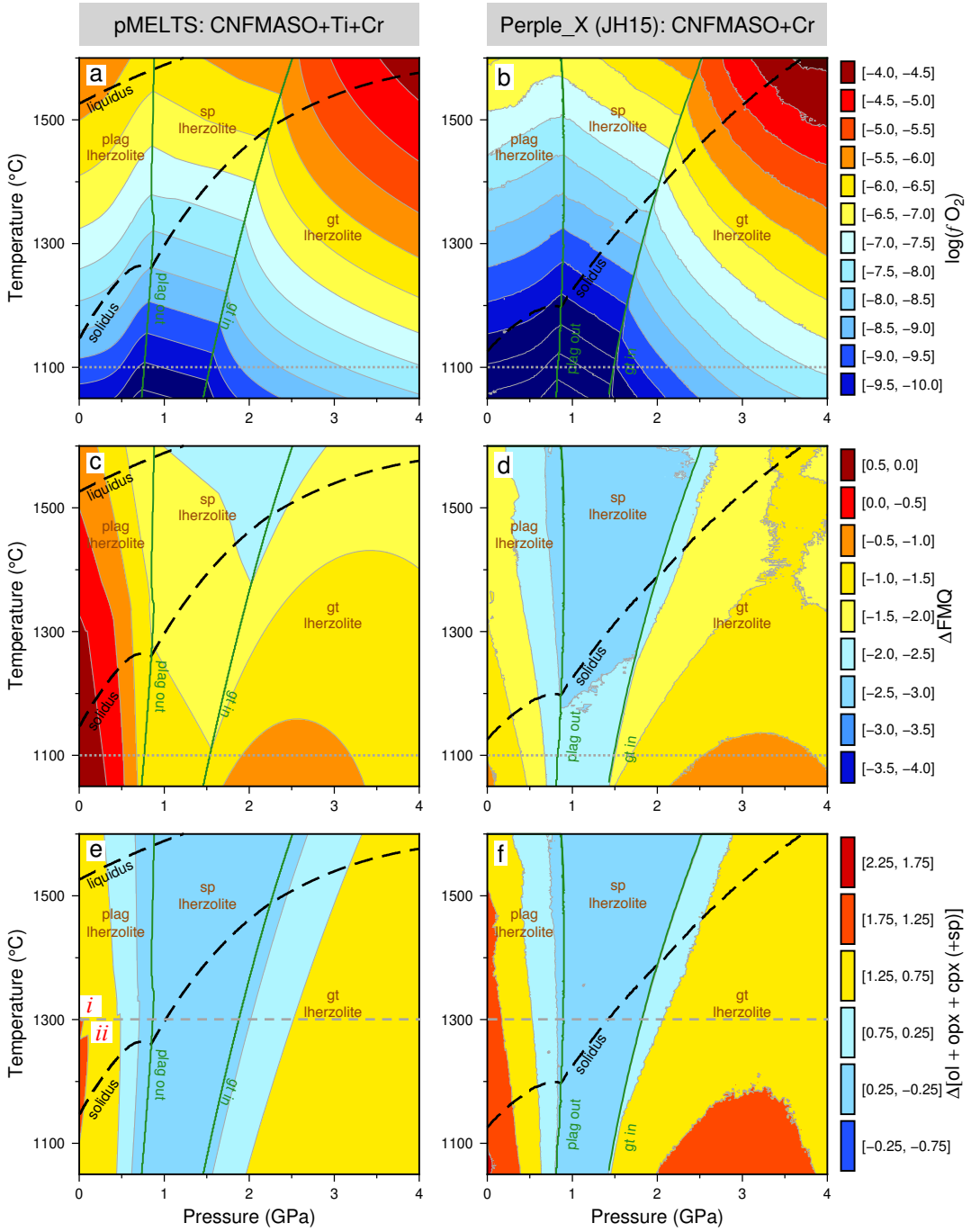
pMELTS: CNFMASO+Ti+Cr
Perple_X (JH15): CNFMASO+Cr
a
b
c
d
e
f
liquidus
solidus
sp lherzolite
plag lherzolite
gt lherzolite
plag out
gt in
i
ii
Temperature (°C)
Pressure (GPa)
log(f O2)
ΔFMQ
Δ[ol + opx + cpx (+sp)]
[−4.0, −4.5]
[−4.5, −5.0]
[−5.0, −5.5]
[−5.5, −6.0]
[−6.0, −6.5]
[−6.5, −7.0]
[−7.0, −7.5]
[−7.5, −8.0]
[−8.0, −8.5]
[−8.5, −9.0]
[−9.0, −9.5]
[−9.5, −10.0]
[0.5, 0.0]
[0.0, −0.5]
[−0.5, −1.0]
[−1.0, −1.5]
[−1.5, −2.0]
[−2.0, −2.5]
[−2.5, −3.0]
[−3.0, −3.5]
[−3.5, −4.0]
[2.25, 1.75]
[1.75, 1.25]
[1.25, 0.75]
[0.75, 0.25]
[0.25, −0.25]
[−0.25, −0.75]

Figure 1

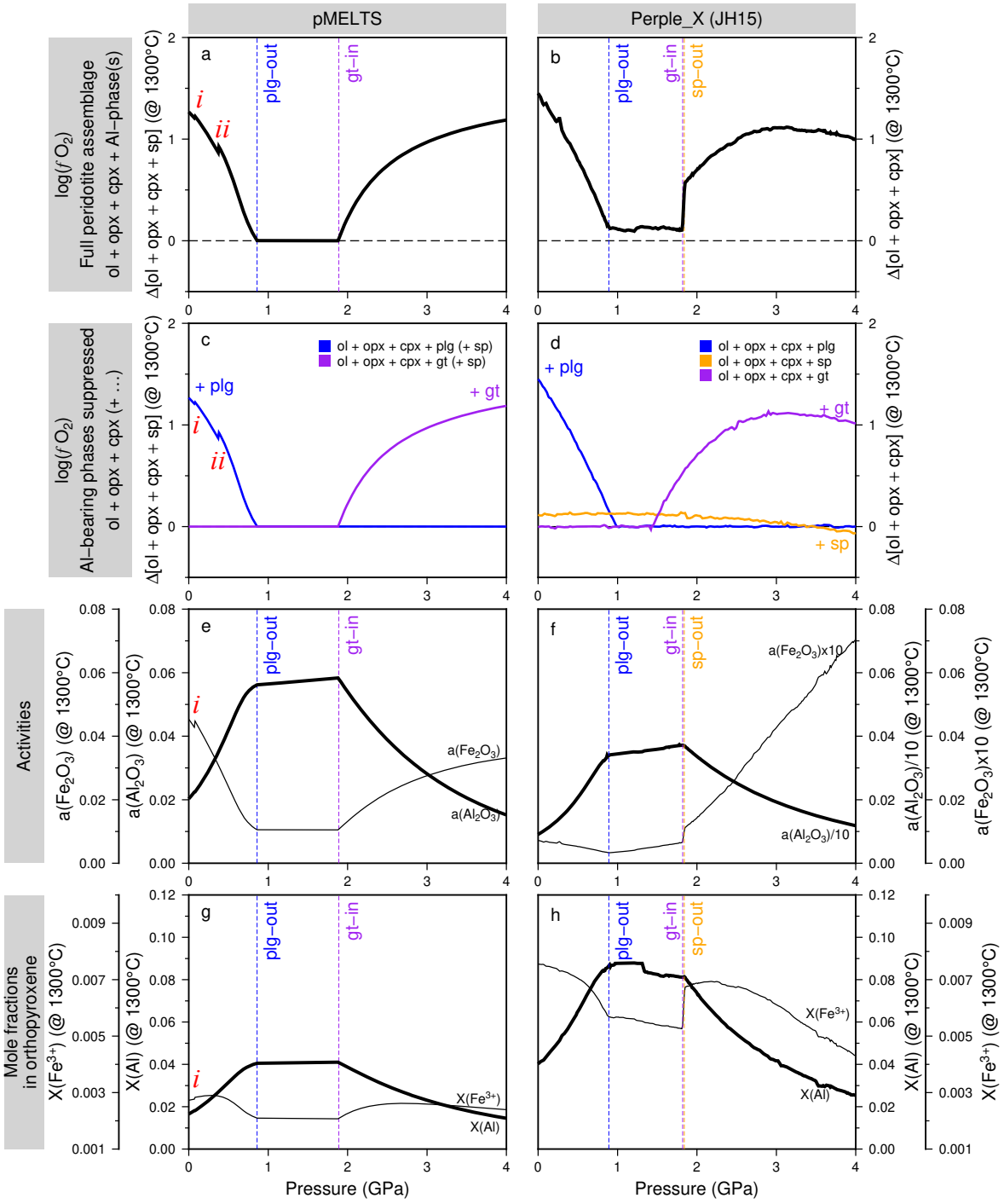
pMELTS
Perple_X (JH15)
log(fO2)
Full peridotite assemblage
ol + opx + cpx + Al–phase(s)
log(fO2)
Al–bearing phases suppressed
ol + opx + cpx (+ …)
Activities
Mole fractions
in orthopyroxene
a
b
c
d
e
f
g
h
i
ii
plg–out
gt–in
sp–out
+ plg
+ gt
+ sp
ol + opx + cpx + plg (+ sp)
ol + opx + cpx + gt (+ sp)
ol + opx + cpx + plg
ol + opx + cpx + sp
ol + opx + cpx + gt
Δ[ol + opx + cpx + sp] (@ 1300°C)
Δ[ol + opx + cpx] (@ 1300°C)
a(Fe2O3) (@ 1300°C)
a(Al2O3) (@ 1300°C)
a(Fe2O3)
a(Al2O3)
a(Fe2O3)x10
a(Al2O3)/10
a(Al2O3)/10 (@ 1300°C)
a(Fe2O3)x10 (@ 1300°C)
X(Fe3+) (@ 1300°C)
X(Al) (@ 1300°C)
X(Fe3+)
X(Al)
Pressure (GPa)

Figure 2

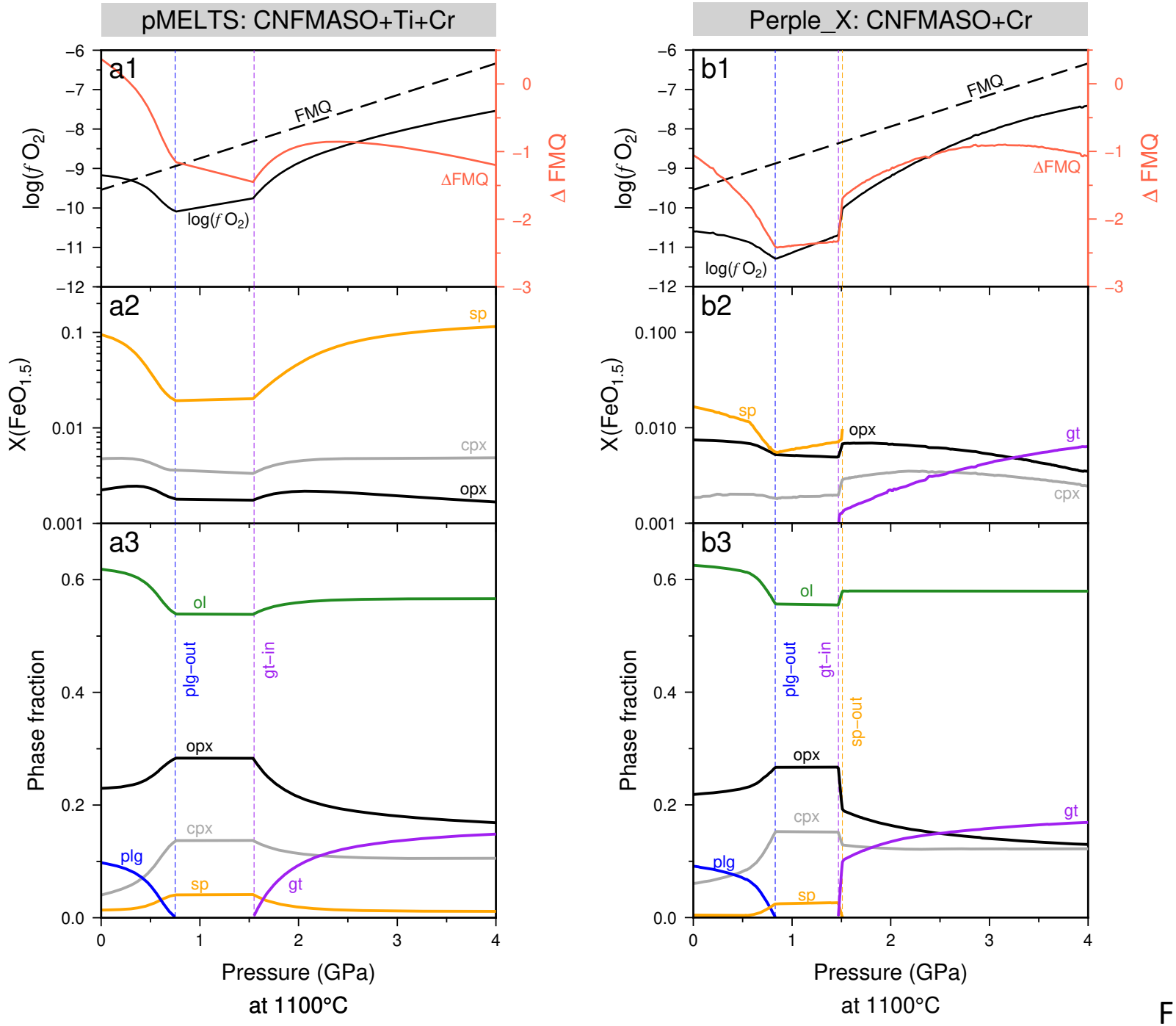
pMELTS: CNFMASO+Ti+Cr
Perple_X: CNFMASO+Cr
a1
b1
log(f O2)
ΔFMQ
FMQ
Δ FMQ
a2
b2
X(FeO1.5)
sp
cpx
opx
gt
a3
b3
Phase fraction
ol
plg
plg–out
gt–in
sp–out
Pressure (GPa)
at 1100°C

Figure 3

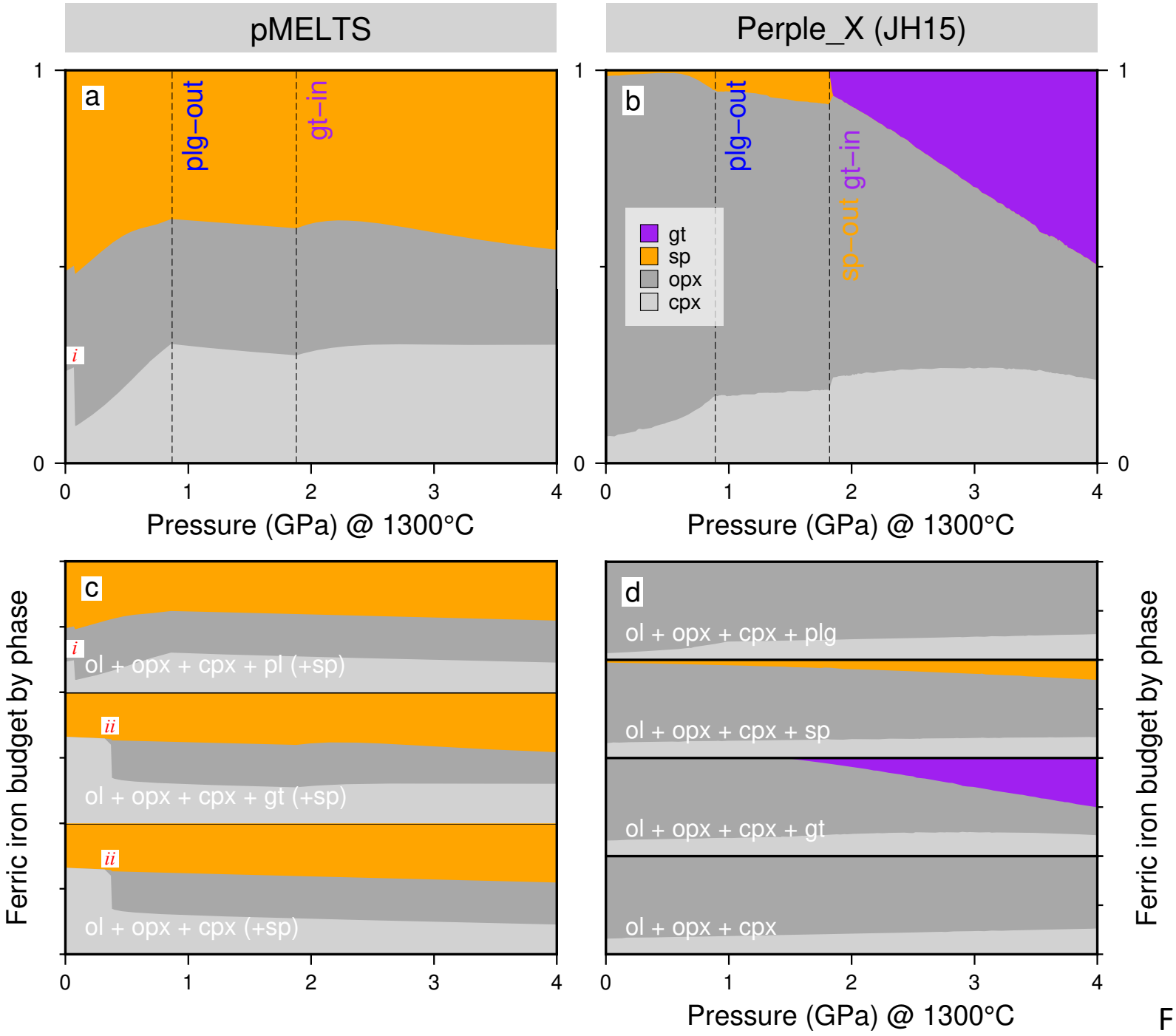
pMELTS
Perple_X (JH15)
a
b
c
d
plg–out
gt–in
sp–out
gt
sp
opx
cpx
i
ii
ol + opx + cpx + pl (+sp)
ol + opx + cpx + gt (+sp)
ol + opx + cpx (+sp)
ol + opx + cpx + plg
ol + opx + cpx + sp
ol + opx + cpx + gt
ol + opx + cpx
Pressure (GPa) @ 1300°C
Ferric iron budget by phase
0
1
2
3
4

Figure 4

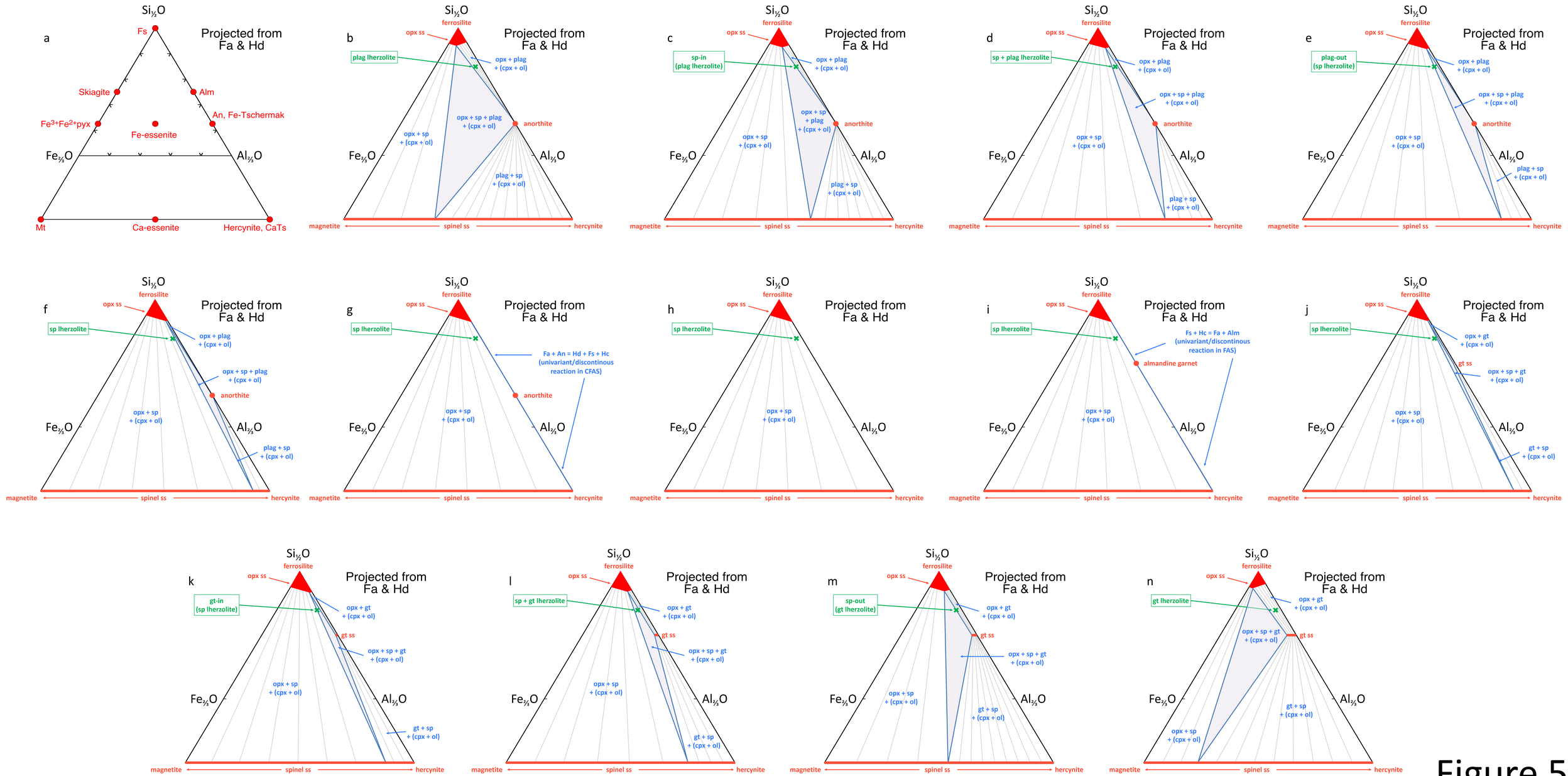
a
Projected from Fa & Hd
Si½O
Fs
Skiagite
Alm
An, Fe-Tschermak
Fe3+Fe2+pyx
Fe-essenite
Fe⅔O
Al⅔O
Mt
Ca-essenite
Hercynite, CaTs
b
c
d
e
f
g
h
i
j
k
l
m
n
ferrosilite
opx ss
plag lherzolite
sp-in (plag lherzolite)
sp + plag lherzolite
plag-out (sp lherzolite)
sp lherzolite
gt-in (sp lherzolite)
sp + gt lherzolite
sp-out (gt lherzolite)
gt lherzolite
opx + plag + (cpx + ol)
opx + sp + plag + (cpx + ol)
opx + sp + (cpx + ol)
plag + sp + (cpx + ol)
anorthite
Fa + An = Hd + Fs + Hc (univariant/discontinous reaction in CFAS)
Fs + Hc = Fa + Alm (univariant/discontinous reaction in FAS)
almandine garnet
opx + gt + (cpx + ol)
opx + sp + gt + (cpx + ol)
gt ss
gt + sp + (cpx + ol)
magnetite
spinel ss
hercynite

Figure 5

a. *plag*-lherzolite facies

b. *gt*-lherzolite facies
(*gt* is pure almandine)

c. *gt*-lherzolite facies
(*gt* is an almandine-skiagite ss)

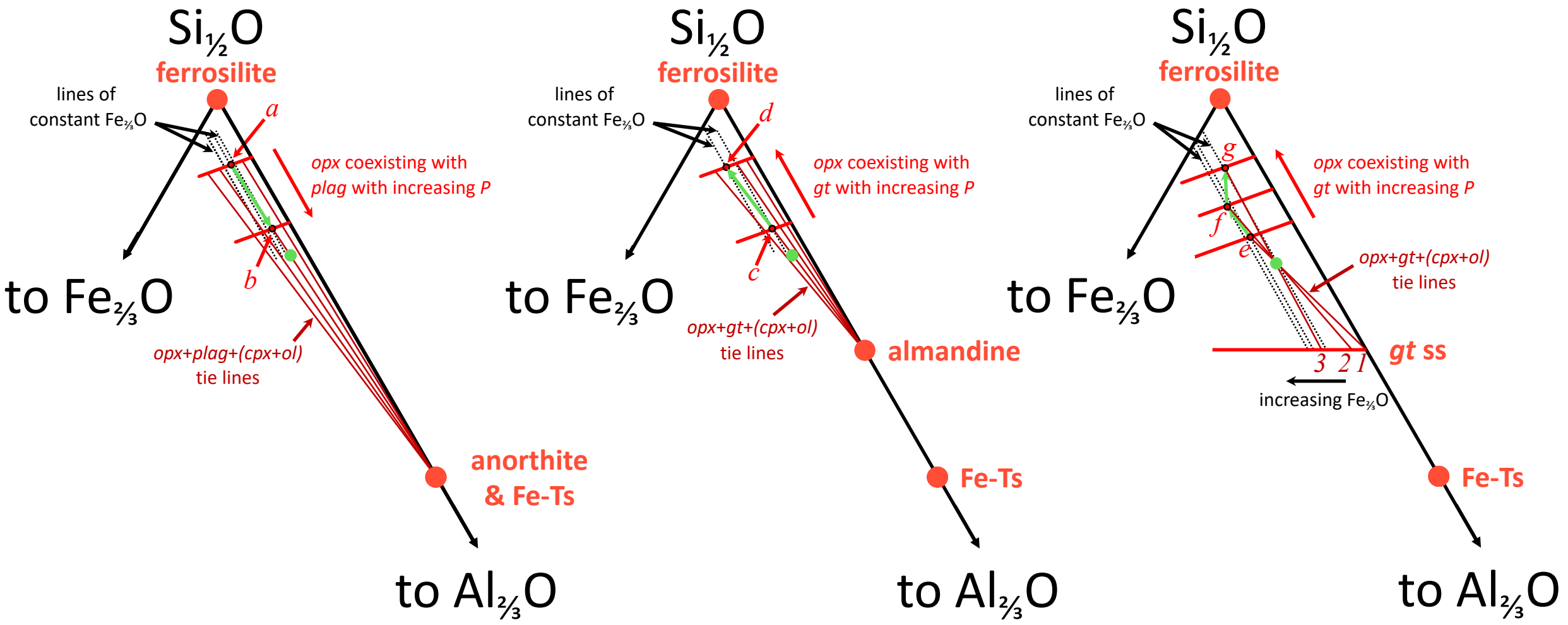

Projected from Fa & Hd

Figure 6